

THESIS

HEAT FLUX TO A WALL IMMERSED IN A RF PLASMA

Submitted by

Justin Wayne Mauck

Department of Mechanical Engineering

In partial fulfillment of the requirements

For the Degree of Master of Science

Colorado State University

Fort Collins, Colorado

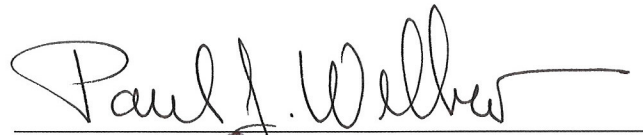
Spring 2008

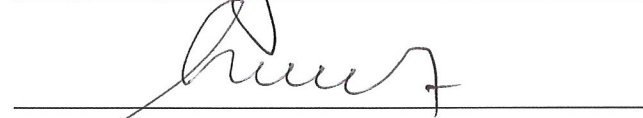
COLORADO STATE UNIVERSITY

April 8, 2008

WE HEREBY RECOMMEND THAT THE THESIS PREPARED UNDER OUR SUPERVISION BY JUSTIN MAUCK ENTITLED HEAT FLUX TO A WALL IMMERSSED IN A RF PLASMA BE ACCEPTED AS FULFILLING IN PART REQUIREMENTS FOR THE DEGREE OF MASTER OF SCIENCE.

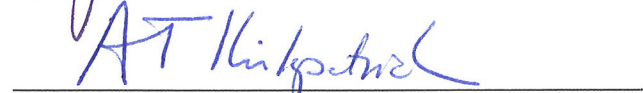
Committee on Graduate work







Adviser



Department Head/Director

ABSTRACT OF THESIS

HEAT FLUX TO A WALL IMMERSED IN A RF PLASMA

A persistent challenge in the design of plasma discharge devices is the removal of heat generated by the plasma that is deposited on the wall of the device. This work is concerned with the deposition and removal of thermal energy on the dielectric wall of an electrodeless, cylindrical inductively coupled plasma (ICP) source of arbitrarily small dimensions. Two methods, not previously reported, are explored which allow the determination of the spatial distribution of heat flux to the plasma facing side of the dielectric tube. Both methods present unique advantages depending on the reactor design. Also included are the applications of these methods to the design of high performance cylindrical ICPs.

Justin Wayne Mauck
Mechanical Engineering Department
Colorado State University
Fort Collins, CO 80523
Spring 2008

ACKNOWLEDGEMENTS

I am extremely grateful to my advisor, John Williams, who provided me with encouragement, patience and valuable input over these past years. I would also like to acknowledge and thank my committee members, Paul Wilbur and Mario Marconi, for their helpful advice. It is my sincere hope we will continue to keep in touch in the future.

I would like to acknowledge Advanced Energy Industries for the funding and flexibility that allowed me to complete this degree. I am fortunate to work for a company that places a high value on education.

I am privileged to work with some very brilliant people in my professional career. I thank Fernando Tomasel and Andrew Shabalin for their dedication and willingness to take personal time in order to contribute to this work. Their support and guidance is very much appreciated and will not be forgotten.

My classmates, Russell Martin and David Alexander, also contributed to this thesis and deserve sincere thanks. I enjoyed getting to know these people.

Finally, I would like to thank J.J. Gonzalez for saying four and a half years ago “Justin, you need to get your Masters” and for not taking “no” for an answer. Without that motivation, I may not be where I am today.

DEDICATION

Dedicated to my loving wife Rose and
two beautiful children Kathryn and James.

Thank you for your support.

TABLE OF CONTENTS

CHAPTER 1	
INTRODUCTION	1
CHAPTER 2	
HEAT FLUX TO THE DIELECTRIC CHAMBER MATERIAL DETERMINED BY CALORIMETRY OF COOLANT TEMPERATURE	15
2.1. Introduction	15
2.2. Experimental Setup	18
2.3. Calculations of Heat Flux Base on Coolant Tube Temperature ..	20
2.3.a. Heat Flux Approximation Using Measured Coil Temperatures (Method 1A)	25
2.3.b. Heat Flux Approximation Including Effects of Temperature Variation Around the Coil Cross-section (Method 1B)	35
2.4. Conjugate Heat Transfer CFD Simulation	46
2.5. Conclusions	51
CHAPTER 3	
HEAT FLUX TO THE DIELECTRIC CHAMBER MATERIAL DETERMINED BY CALORIMETRY OF DIELECTRIC TEMPERATURE	53
3.1. Introduction	53
3.2. Experimental Setup	55
3.3. Calculation of Heat Flux Based on Dielectric Wall Temperature Rise	61

CHAPTER 4	
APPLICATION OF HEAT FLUX DISTRIBUTION DATA IN REACTOR DESIGN	73
4.1. Introduction	73
4.2. Experimental Reactor Failure	74
4.3. Thermal-Mechanical Reactor Design Using Finite Element Analysis	76
 CHAPTER 5	
CONCLUSIONS	80
 APPENDIX A	
Isobaric Water Properties at 15 psia as Function of Temperature	82
 APPENDIX B	
Thermal Capacitance of Fused Quartz as Function of Temperature	86

CHAPTER 1

INTRODUCTION

This work is concerned with the deposition and removal of thermal energy on the dielectric wall of an electrodeless, inductively coupled plasma source used in industrial applications for etching, cleaning and chemical processing. A persistent challenge in the design of such plasma discharge devices is the removal of heat generated by the plasma that is deposited on the wall of the device. The performance of many industrial processes such as plasma enhanced chemical vapor deposition, plasma etching and cleaning, spray deposition and sputtering, as well as the operation of plasma devices such as nuclear fusion reactors, to name a few, depend critically on the energy balance between the plasma and the wall or boundary that confines the plasma. The thermal conditions at the surfaces exposed to the plasma play a central role in the plasma-wall interaction, as they critically affect elementary processes including deposition, adsorption, desorption, diffusion, and chemical reactions that are strongly dependent on temperature. In the case of the extremely high heat loads commonly found in fusion reactors, the plasma facing materials suffer from degradation due to vaporization, sublimation, spallation, sputtering, ... , with erosion rates that are also highly dependent on surface temperature and, hence, on the balance between heat deposition and removal.

Over the past several decades there has been intensive research regarding the energy transport and heat balance on a large number of different plasma

source applications ranging from wafer processing to fusion reactors, including theoretical [Hildebrandt, Naujoks, and Sünder, 2005; Takaki, Koseki and Fujiwara, 2001; Takaki, Koseki, and Fujiwara, 2001; Eich, et al., 2003; Herrmann, et al., 1995; Lott, et al., 2005] and experimental [Federici and René Raffray, 1997; Blanchard, 1994; Yeh, 2006; Kersten, 2001; Martz, Hess, and Petersen, 1992; You and Bolt, 2001] approaches. In most cases of interest, the energy transfer between plasmas and surfaces is a very complicated problem for which self-consistent, quantitative models are virtually non-existent for most situations. For the particular case of low-temperature, high-pressure equilibrium plasmas created in monatomic gases the problem is somewhat simpler, and the transfer can sometimes be described by means of classical heat transfer concepts such as thermal conductivity and heat transfer coefficients. The modeling becomes considerably more complex, however, by just replacing the monatomic gas by a molecular gas.

The description of non-equilibrium, low-pressure plasmas is much more challenging because in these plasmas the classical treatment of heat transfer is no longer adequate, and the thermal conditions at the surface must be described by a detailed energy balance that takes into account the plasma production, diffusion, absorption, recombination and neutralization processes that occur nearby and on the surface. The main contributions of energy flux to a surface include radiation towards the surface, the power transferred by charged species (electron and ions), the contribution of neutral species, the energy released on the surface by adsorption and particle de-excitation, and the reaction energy from exothermic

processes, including recombination and chemical etching. Energy loss processes include radiation from the surface, heat loss by conduction and convection, desorption, and endothermic reactions. The complexity of the problem makes the integration of plasma discharge chemistry and physics with energy transport in a self-consistent model a formidable task, even for the case of a global model. Particular cases for which models can be more easily solved are sometimes of academic interest but of little help in the design of plasma chambers, especially in the case of multipurpose reactors that need to be designed to run with a wide variety of gas species, flow rates, plasma power levels and pressures.

The study of heat deposition and removal in plasma devices is particularly important in the case where the materials exposed to the plasma serve structural purposes where they must hold off atmospheric pressures while not developing leaks. In this case, the inability of materials exposed to plasmas to withstand the thermal environment of the discharge often significantly restricts the performance, range, reliability, or other operating characteristics of a plasma reactor. Problems of thermal management are especially difficult in high-power reactors having structural dielectric materials with poor thermal conductivity properties in close proximity to the plasma. While certain dielectric materials such as ceramics may be tolerant of elevated uniform temperatures, non-uniform heat distributions (i.e. temperature gradients) can lead to intolerable internal stresses due to differential thermal expansion. In fact, it is not uncommon for these temperature gradient-induced stresses to result in cracks in dielectric materials, leading in turn to premature and in some cases catastrophic failure of the plasma reactor. The

situation is particularly critical in the case of electrodeless, inductively-coupled plasma (ICP) sources operating at relatively low pressures, in which a large fraction of the power is deposited to the dielectric walls, the topic of this thesis.

ICP discharges, especially for applications related to materials processing, have been described in high detail in the literature (eg., Lieberman and Gottscho, 1994 and references therein). Figure 1.1 shows a schematic representation of two of the simplest and most popular configurations. For these reactors, the ICP chamber consists of an RF antenna either wrapped around a cylinder or as a spiral “electric stove-top” shaped structure placed in close proximity to a dielectric tube or window that is part of a vacuum chamber. The electromagnetic RF fields created by the antenna initiate and sustain a plasma inside the chamber, where the pressure is typically less than a few Torr. The plasma acts as the single-turn, lossy secondary of an air-coupled transformer whose primary winding is the multi-turn or spatially curvy RF antenna. In these discharges the power coupling efficiency depends critically on the proximity of the RF antenna to the plasma.

Inductive electrodeless discharges have been studied for more than a century, although their widespread use for materials processing is rather recent. The study of these plasma discharges was initiated in the late eighteenth century with the work of Hittorf (1884). The phenomenon was subsequently examined by a number of researchers, in particular by J.J. Thomson (1927). The experiments performed on electrodeless discharges during their early discovery period (1920-1936) used quartz or glass vessels and relatively low power supplies. The

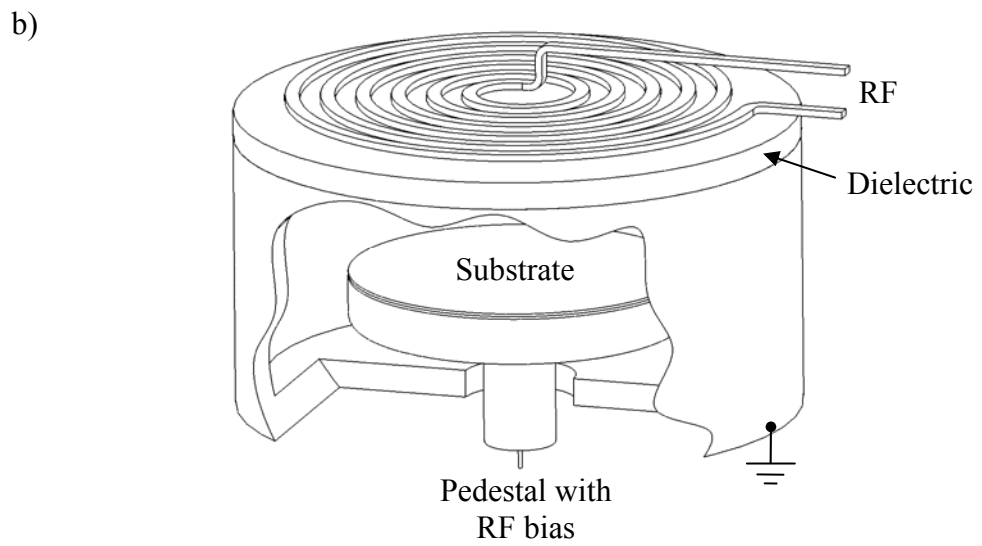
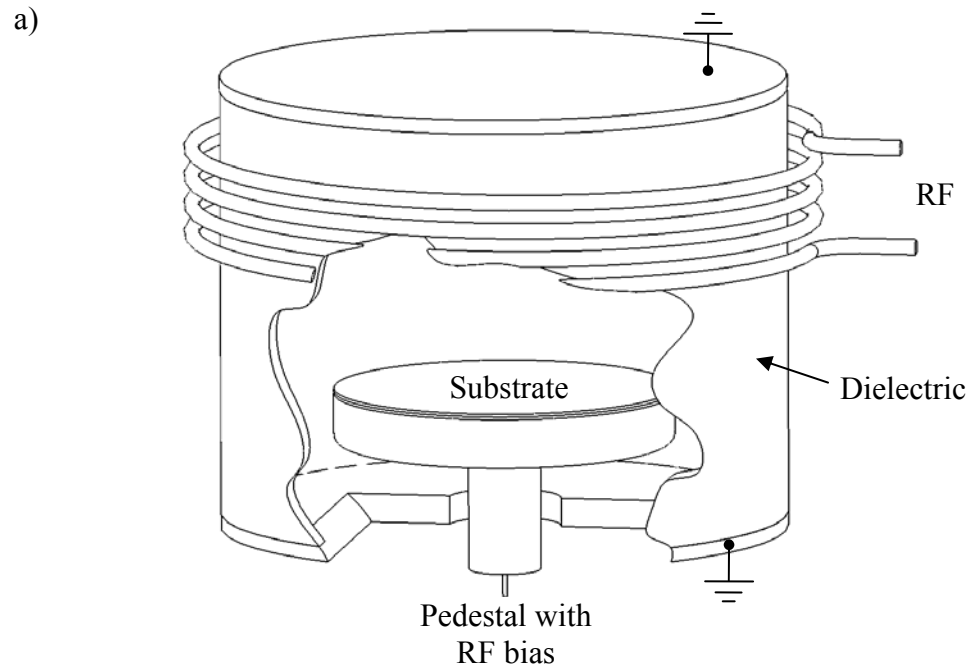


Figure 1.1 Schematic representation of inductively driven sources in a) cylindrical and b) planar geometries. [Adapted from Lieberman and Gottscho, 1994]

motivation for these studies was mainly academic, aimed to the understanding of the underlying physics of the discharges, and no practical applications for this technology were foreseen. Later experiments, however, at much higher powers performed by Babat (1947) using RF vacuum tube oscillators enabled the use of electrodeless discharges in a number of applications, starting with spectroscopy [Nisewanger et al., 1946], and production of positive ions [Thonemann, 1948]. Continued investigation of cylindrical, inductive discharges eventually allowed for the development of plasma reactors in which low temperature plasmas could be generated and sustained. Limitations on the maximum power load that dielectric chambers were able to withstand led to the development of inductive discharge chambers with water-cooled, slotted metallic walls [Mironer, 1963].

Most of the development of low pressure inductive plasma sources during the last two decades has been fueled by developments in the semiconductor industry. In typical wafer processing reactors, such as those schematically shown in Figure 1.1, the total RF power delivered to the ICP coil may be relatively high, reaching values of 5 kW. The volume of the chambers for in-situ inductive plasma processing is fairly large, however, and, as a consequence, the maximum power density for typical semiconductor processing chambers is of the order of 1 W/cm^3 . The situation is different in the case of remote plasma production, an alternative plasma production scheme that has gained increased acceptance in semiconductor processing.

Remote plasma production is used in an increasing number of applications ranging from chamber cleaning to photoresist and native oxide removal, reducing

both wafer damage and chamber wear. In remote plasma production, the plasma is created in a separate chamber and the byproducts of the plasma (usually neutrals, including radicals and atomic species) are then brought into the main wafer processing chamber via vacuum ports and showerheads. Remote plasma reactors are much smaller than wafer-processing chambers, and, for plasma production to be effective, the power densities required are usually considerably higher than those used for in-situ processing. In present day applications, the design goals for average volumetric and surface heat loads for remote ICP sources are about 10 W/cm^3 and 10 W/cm^2 , respectively. These and other requirements, such as chemical compatibility, low surface recombination rates, and constructive simplicity, make the design of high-performance remote plasma sources a formidable challenge. Due mainly to these constraints, commercial remote ICP reactors currently available have been limited to approximately 600 W for 50 mm diameter, 300 mm long cylindrical chambers.

A fairly new application for low-pressure ICP reactors is the abatement of environmentally unfriendly greenhouse gases used for wafer processing. Current environmental concerns about global warming have prompted tighter regulations on the allowable emissions of greenhouse gases, and the semiconductor industry is no exception. Many of the gases used for etching are perfluorinated, including perfluorocarbons (e.g. CF_4 , C_2F_6 and C_3F_8), hydrofluorocarbons (e.g. CHF_3), and sulfur hexafluoride (SF_6). These gases are considered to have a high global warming impact because of their strong infrared absorption cross sections and long atmospheric lifetimes, which can be as long as 50,000 years for CF_4 , for

example [Tonnis, 2000]. While efforts have been made to reduce the use of these potent greenhouse gases in the semiconductor industry, the increasing demand on consumer electronics and the unavailability of safe and cost-effective alternatives require new ways of processing the exhaust of the semiconductor processing tools to decrease the greenhouse potential of their emissions.

Different abatement alternatives are available including natural gas burners, catalytic traps, and microwave discharges, all of which operate at atmospheric pressure at the outlet of the vacuum pumping stations. However, there has been an increasing interest in developing relatively high power plasma discharges that could do in-line abatement before the gases reach the mechanical pumps. These plasma reactors operate at pressures of several hundred millitorrs, and need to be compact enough to be installed directly in the pumping foreline. Also, they need to have a large enough chamber diameter so as not to impede the physical conductance of the gas through the foreline. Similar to the remote plasma sources used on the wafer processing chambers, the abatement plasma sources need to be compact, chemically resistant to fluorine and other highly corrosive gases, and able to deliver relatively high powers (typically between 1.5 and 4.5 kW for typical recipes currently used in 300 mm wafer chambers).

The challenges faced by the designers of cylindrical, inductively coupled plasma sources are common to other high-power, low-pressure plasma sources such as toroidal, transformer-coupled reactors. Figure 2 shows a simplified view of one of these reactors. In this configuration, a toroidal plasma vessel runs through the center of a magnetic core. A multi-turn winding wrapped

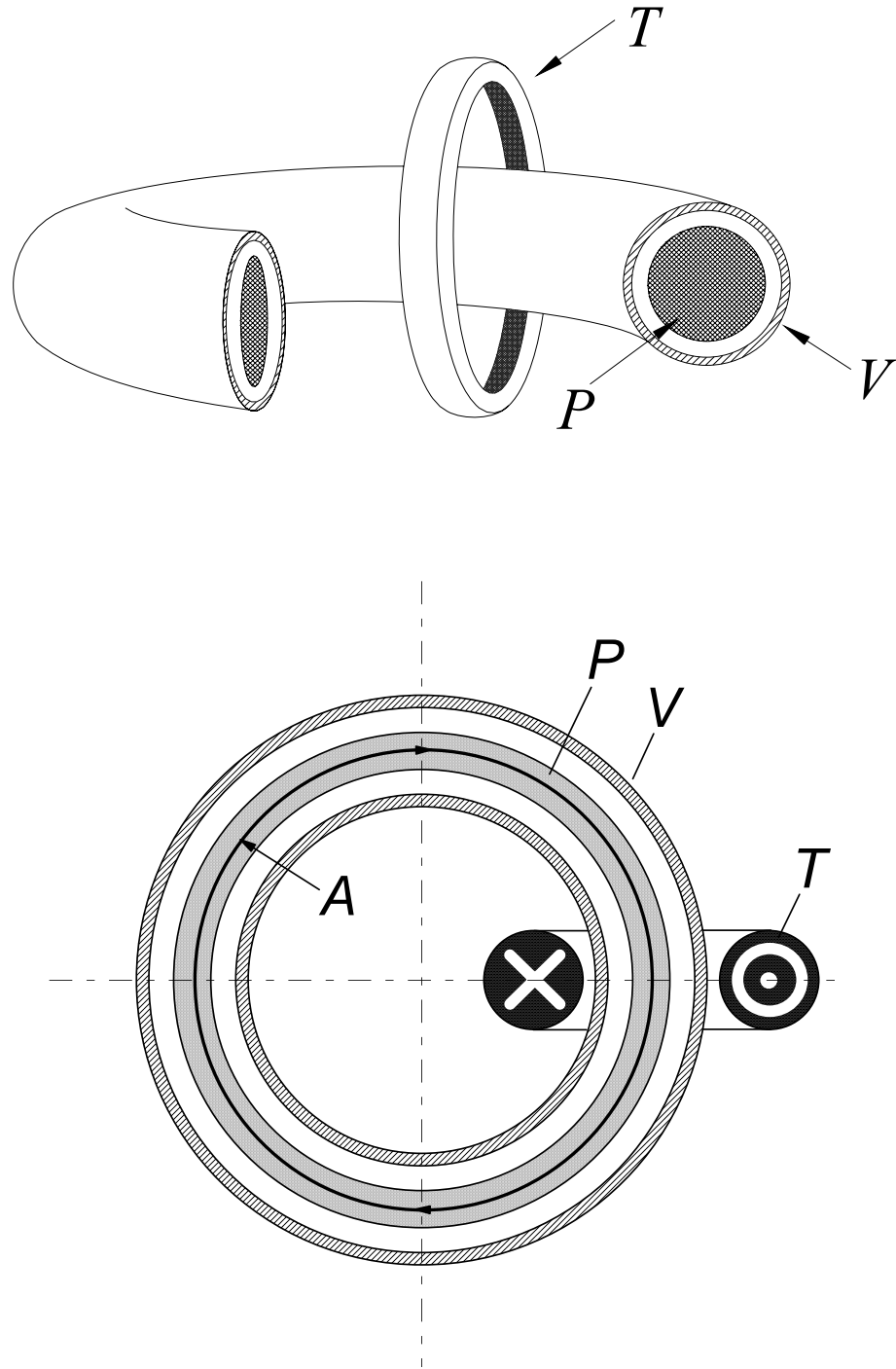


Figure 1.2 Isometric and cross sectional views of the toroidal chamber. Letters V , P and T indicate the vessel, plasma column and toroidal ferrite core, respectively. For simplicity, no other elements, such as the primary coil, are drawn. [From Gonzalez (2005)]

around the core serves as the primary of the transformer, while the plasma ring formed inside the chamber works as a single-turn secondary winding. These plasma discharges were first studied by Ware and Cousins at the Imperial College, and by Thonemann at Oxford around 1947 [see Hendry and Lawson, 1993 and references therein], as part of investigations motivated by the possibility of producing high temperature plasmas suitable to achieve nuclear fusion. Dielectric vessels were also used as a starting point for these investigations. Using a glass torus and a 7 kW, 100 kHz power oscillator, Thonemann was able to successfully generate plasmas with currents of up to several tens of amperes. Nevertheless, it became clear that the high currents needed for fusion experiments could not be sustained in dielectric chambers, due to poor thermal properties of the dielectric materials and difficulties in achieving efficient cooling of the chamber walls.

As in the case of the high-power cylindrical discharges, the solution proposed was to use a torus with metal walls, provided with dielectric gaps that impeded the generation and circulation of eddy current loops on the walls. These rather simple toroidal chambers rapidly evolved into much more sophisticated plasma confinement schemes, such as tokamaks and stellarators. In the last few decades, scientists have scaled up the power of experimental toroidal reactors to plasma currents of 15 MA and powers of hundreds of megawatts. As an example, the peak volumetric heat load in the structure and the surface heat flux for the first wall of the International Thermonuclear Experimental Reactor (ITER) are expected to be of the order of 20 W/cm^3 and 20 W/cm^2 , respectively. Notice that

these values for a multi-billion dollar research device are only a factor of two above the design goal of current remote ICP sources.

Due to a sustained high level of funding motivated by the potential of fusion reactors, it is in the design of high-power, fusion-oriented inductive plasmas where most of the development of plasma facing materials and structures has occurred in the last two decades. For initial feasibility studies, all experimental fusion reactors were operated in a pulsed mode. Larger fusion reactors currently under design or construction will operate under steady state conditions, however, high temperature ceramic tiles will be brazed to the actively cooled underlying structure to help the wall survive. Currently, surface temperature and power deposition measurements on candidate wall materials are performed using thermography and calorimetry. Although the experimental setups vary somewhat depending on the plasma machine being analyzed, they all rely on infrared imaging of test plates immersed in the plasma. These setups are adequate for large scale reactors, where the test plates do not disturb the plasma significantly, and where the spatial profile of the plasma load can be mapped by changing the position of the plate along the internal wall. Since the wall heat load conditions in ICP sources are similar, it would be highly desirable to use fusion wall diagnostics in the evaluation of high-power, compact inductive plasma sources, but due to size limitations, the methods and experimental setups of fusion wall studies cannot be readily implemented.

This thesis provides two methods not previously reported in the characterization of high performance inductive plasma sources. Both methods

allow determination of the spatial distribution of heat flux to the plasma facing side of the dielectric tube used in a cylindrical ICP reactor of arbitrarily small dimensions. And both methods present unique advantages depending on the reactor design, and, although motivated and developed for the particular case of cylindrical chambers, these methods can also be used in the study of chamber configurations other than cylindrical. The thesis is organized as follows: Chapter 2 describes the first method, for which the heat flux is determined from spatially-resolved, steady-state measurements of the temperature rise in the cooling fluid as it travels through the tubing wrapped around the plasma chamber. Chapter 3 presents a second method, where the heat flux is calculated from space- and time-resolved measurements of the temperature rise of the dielectric chamber as a function of time after the plasma is initiated. Chapter 4 demonstrates the use of these methods and presents rules for the design of high performance cylindrical ICPs. Chapter 5 summarizes the results, compares the relative advantages and disadvantages of both approaches, and identifies areas of interest for future work.

REFERENCES

- Andrew, P. et al. (2003), *J. Nucl. Mater.* **313-316**, 135-139.
- Araki, M. and Kobayashi, M. (1996), *Rev. Sci. Instrum.* **67**, 178-184.
- Babat, G. I. (1947), *J. Inst. Elec. Eng. (London)* **94**, 27-37.
- Blanchard, J. P. (1994), *J. Vac. Sci. Technol. B* **12**, 910-917.
- Bolt, H. et al. (1998), *Fusion Eng. Des.* **39-40**, 287-294.
- Eich, T. et al. (2003), “Power Deposition Measurements in Deuterium and Helium Discharges in JET MKIIGB Divertor By IR-Thermography”, European Fusion Development Agreement, EFDA-JET-CP(02) 01/03.
- Eich, T. et al. (2003), *J. Nucl. Mater.* **313-316**, 919-924.
- Gonzalez, J.J. (2005), “Study of transformer coupled toroidal discharges”, PhD Dissertation, Colorado State University.
- Federici, G. and René Raffray, A. (1997), *J. Nucl. Mater.* **244**, 101-130.
- Hendry, J. and Lawson, J. D. (1993), “Fusion Research in the UK 1945-1960”, United Kingdom Atomic Energy Authority.
- Herrmann, A. et al. (1995), *Plasma Phys. Control. Fusion* **37**, 17-29.
- Hildebrandt, D., Naujoks, D. and Sünder, D. (2005), *J. Nucl. Mater.* **337-339**, 1064-1068.
- Hittorf, W. (1884), *Ann. Phys.* **21**, 90-139.
- Kersten, H. et al. (2001), *Vacuum* **63**, 385-431.

- Lieberman M. A. and Gottscho R. A. (1994), Design of high-density plasma a sources for materials processing, *Physics of Thin Films*, **18**, Francombe M. H. and Vossen J. L. eds., Academic, New York.
- Lott, F. et al. (2005), *J. Nucl. Mater.* **337-339**, 786-790.
- Martz, J. C., Hess, D. W. and Petersen, E. E. (1992), *J. Appl. Phys.* **72**, 3283-3288.
- Mironer, A. (1963), *AIAA J.* **1**, 2638-2639.
- Nisewanger, C.R., Holmes, J. R., and Weissler, G. L. (1946), *J. Opt. Soc. Am.* **36**, 581.
- Takaki, K., Koseki, D. and Fujiwara, T. (2001), *Surf. Coat. Technol.* **136**, 261-264.
- Thomson, J. J. (1927), *Phil. Mat. Ser. 7* **4**, 1128-1160.
- Thonemann, P.C., Moffat, J., Roaf, D., and Sanders, J. H. (1948), *Proc. Phys. Soc. Lond.* **61**, 482.
- Tonnis, E. et al. (2000), *J. Vac. Sci. Technol. A* **18**, 393-400.
- Yeh, F. B. (2006), *Int. J. Heat Mass Transfer* **50**, 789-798.
- You, J. H., Bolt, H. (2001), *J. Nucl. Mater.* **299**, 9-19.

CHAPTER 2

HEAT FLUX TO THE DIELECTRIC CHAMBER MATERIAL DETERMINED BY CALORIMETRY OF COOLANT TEMPERATURE

2.1. Introduction

This chapter describes a calorimetric-based approach (to be referred to as Method 1) where the spatially resolved rise in the temperature of coolant circulating through the cooling system of a plasma chamber is used to estimate the power deposited on the chamber walls. This method is meant in particular for reactors that have very good thermal coupling to the coolant and a high density of coolant tubing in contact with the dielectric. In these experiments, a commercial remote plasma source (RPS) developed by Advanced Energy Industries is utilized. The RPS, model LB3001, consists of an integrated ICP reactor and 3000 W radio-frequency (RF) power supply. The semiconductor industry uses this integrated plasma source for a variety of front-end processes as well as in gas abatement applications at the back end. The reactor chamber consists of a 70 mm diameter and 250 mm long structural, dielectric tube wrapped by a cooled coil of square copper tube through which water is flowed. The length of copper tube used to make the coil is approximately 3.71 meters. The reactor is manufactured in such a way that the cooling coil has very good thermal contact with the chamber material. The coil also serves as the RF antenna to initiate and sustain a plasma inside the chamber tube, and is electrically isolated from the rest of the unit. The plasma source can be manufactured with two different dielectric

chamber materials: ceramic alumina (Al_2O_3) or quartz (SiO_2). The assembly is completely encapsulated (i.e. potted) with a silicon potting compound. Figure 2.1 (a) shows the general construction of the chamber, with the encapsulant removed for clarity.

The power supply on the RPS consists of DC and RF sections. The DC section converts 50-60 Hz AC power into regulated DC power used to feed the RF section. In the RF section, the DC power is converted to RF frequency of 1.9 MHz to 3.2 MHz and is in turn delivered to the plasma via the coil antenna. The total power to the plasma varies widely depending on the plasma conditions, which strongly affects the efficiency of RF generation. Because of this, the power efficiency of the RF section is not always exactly known, but is in the range of 70% - 80%, and the actual RF power delivered to the sustained plasma is in the range from 2100 to 2400 W.

To determine the heat flux from the plasma to the wall, the reactor was modified by removing a section of the encapsulant to expose the coolant coil, as illustrated in Figure 2.1 (b). The exposed section of coil allows for surface temperature measurements that are subsequently used in calculations of the heat flux as detailed later in this Chapter. The heat transfer arrangement shown in Figure 2.1 is similar to a combustion heat exchanger where the plasma can be viewed as the combustion zone and the coils as the energy absorbing elements.

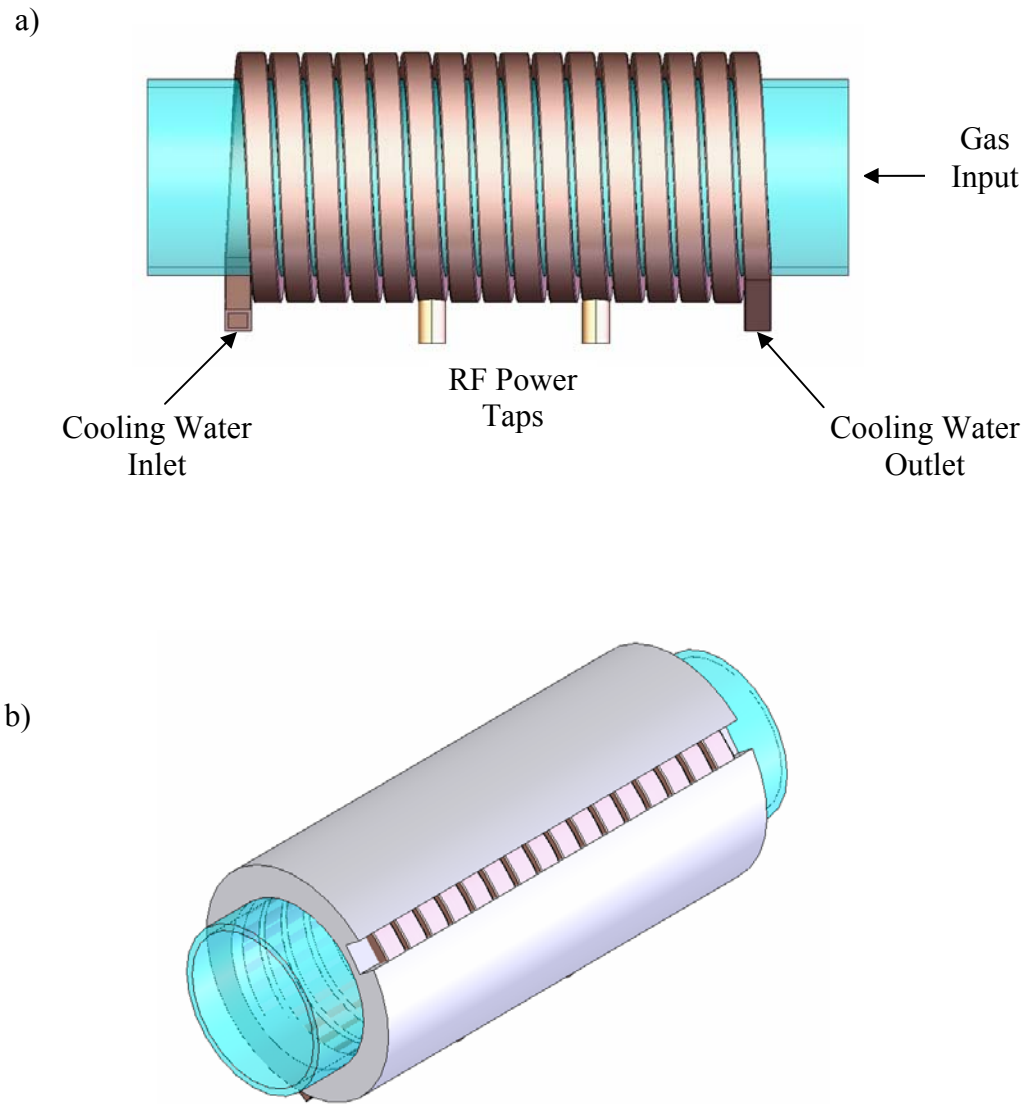


Figure 2.1 a) Side view illustration of the chamber with the encapsulant removed for clarity. The gas flow direction and power connections are shown. b) The chamber section isometric view with a section of the encapsulant removed to expose the coolant coil.

2.2. Experimental Setup

Coil temperatures were obtained using a FLIR S40 thermal imaging infrared camera. The camera is set up with an unobstructed view of the entire area where the encapsulant has been removed. Due to the poor emissivity of copper, it was painted with high emissivity paint to improve the accuracy of the thermal measurements. Cooling water flowrate, inlet temperature, outlet temperature, and temperature along the coil were simultaneously monitored while the unit was producing plasma. The temperature of the coil is allowed to rise until steady state conditions were achieved. This usually takes about 5 minutes, depending on the coolant flow rate and plasma power level. As the dielectric heats up, thermal energy is transferred to the copper tube and then to the water, and, consequently, the water temperatures increases. The heated water moves through the tube at a nearly constant mean velocity dictated by the flow rate, density, and cross-sectional area of the tubing. Thermal images of a typical experimental run are shown in Figure 2.2 where the thermal conditions at two times during the same run: 10 seconds after starting the source Figure 2.2 (a) and 3 minutes after starting Figure 2.2 (b). It is noted that the images have different temperature scales. The calorimetric method described here uses the steady-state temperature profile along the coil to calculate the heat flux from the plasma. The next sections will show how these calculations are performed for a particular plasma condition.

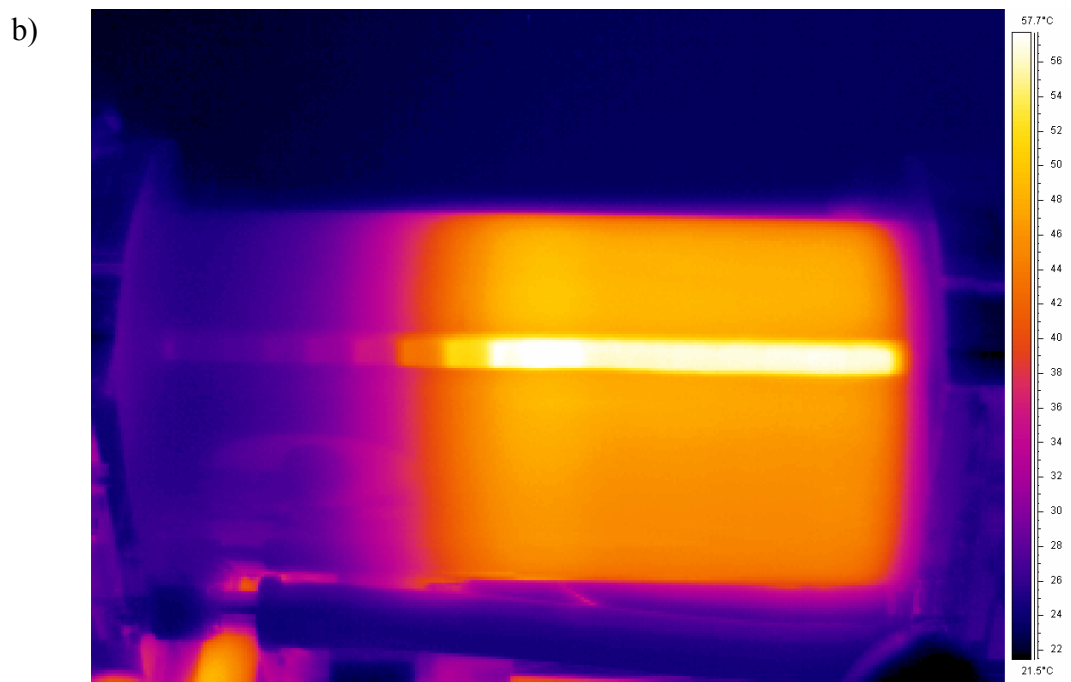
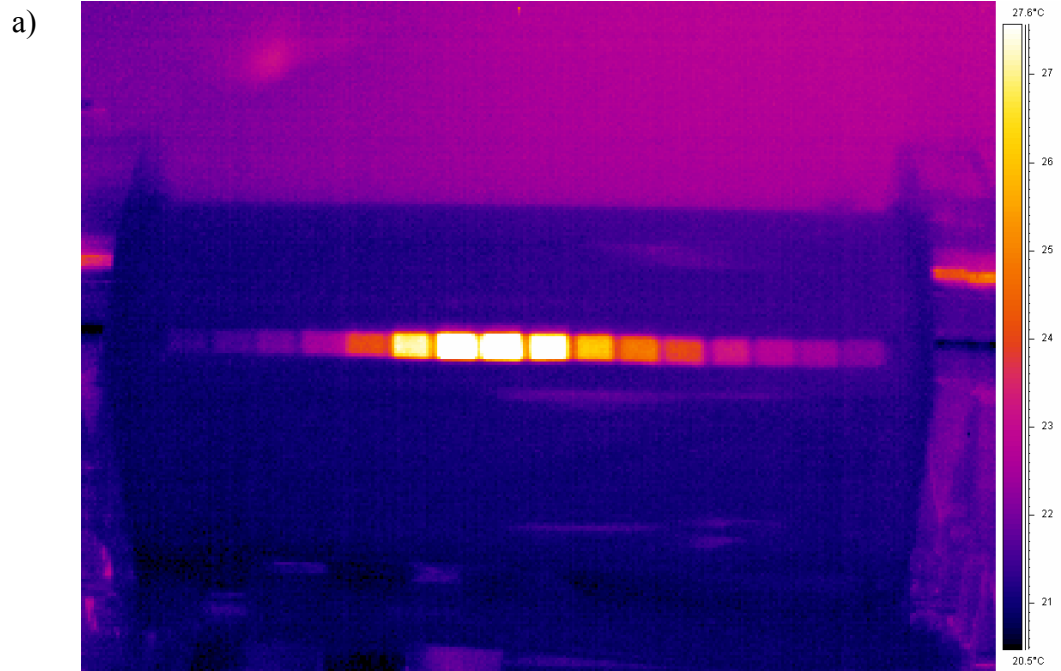


Figure 2.2 a) Thermal image taken 10 seconds after the plasma source was turned on. b) Thermal image of the same experimental run after 3 minutes of plasma source operation. These two images have different temperature scales.

2.3. Calculations of Heat Flux Based on Coolant Tube Temperature

The heat deposited on the internal chamber wall will cause a rise in the temperature of the coolant as it circulates through the system. The change in temperature can be used to estimate the spatially varying heat flux, but first one must find the coolant properties as a function of temperature because the bulk change in temperature can be somewhat significant. The coolant fluid is water for all the tests described herein.

Experimental data show a condition where the plasma produces a very intense heat flux region that is concentrated between the RF power connections. This situation occurs with a high power, relatively high pressure, O₂ plasma. For comparison of the calculations in this thesis, the plasma operating conditions will always be as follows:

Power level: 3000 W*

Gas: O₂

Gas Flow: 750 sccm

Pressure: 2 Torr

* Power delivered to the RF section

Isobaric properties for water at 15 psia from 0.01°C to 100.01°C are gathered from the National Institute of Standards and Technology (NIST) database and compiled in Appendix A. They include the thermal conductivity k in $\text{W}\cdot\text{m}^{-1}\cdot\text{K}^{-1}$, density ρ in $\text{kg}\cdot\text{m}^{-3}$, dynamic viscosity μ in $\text{Pa}\cdot\text{s}$, kinematic viscosity ν in $\text{m}^2\cdot\text{s}^{-1}$, and specific heat at constant pressure C_p in $\text{J}\cdot\text{kg}^{-1}\cdot\text{K}^{-1}$. The kinematic viscosity is calculated using Equation 2.1 [see Munson, Young and Okiishi, 1990]

using the NIST dynamic viscosity and density data, which are functions of the water temperature, T_w .

$$\nu(T_w) = \frac{\eta(T_w)}{\rho(T_w)} \quad (2.1)$$

The coil geometries are known and detailed in Figure 2.3. As briefly described before, the chamber coolant circuit consists of a 9.5 mm square tube coiled around the dielectric chamber, in this case a quartz tube. There are 16 turns of the coil with the RF power connections on turns 6 and 11. The coil pitch is 11.1 mm and results in a region of dielectric 176.5 mm long with coil wrapped around. It is within this region where the heat flux is calculated (except for a $\frac{1}{2}$ turn on each end where the heat flux is not calculated). This results in a region where power deposition is assumed to occur that is 167.1 mm long, refer to Figure 2.3 (b) for an illustration. The total reactor length is 244.9 mm, so there are regions on each end of the dielectric tube where the heat flux is not calculated. This assumption is valid because there is negligible power expected to be deposited in these regions when the plasma source is operated in an inductive mode. The plasma region is divided into 15 sections and the heat flux is calculated and assumed constant for each section based on the temperature rise of the coil in that section. Each section width is defined as the distance between the midpoints of each coil turn, or equivalently the pitch of the coil.

Water temperatures are taken for various flow rates while the unit is generating the O₂ plasma in the conditions mentioned above. When the

temperatures reach steady state, they are recorded for each of the 15 coil locations. The flow rates used in these experiments are bound on the lower side by the necessity to properly cool the unit and on the upper side by the accuracy of the thermal measurements. If the water flow is too low, the unit will overheat and cause damage to the power supply or the reactor wall. This lower limit is 0.2 GPM. If the water flow is high, the temperature change from coil to coil becomes small and not easily distinguishable by the thermal camera. The upper limit is 0.6 GPM. Data are gathered in this range at 0.1 GPM increments. These data are curve fit and plotted in Figure 2.4 as a function of distance along the coolant coil. The temperature rise along the coil length can now be used to calculate the heat flux from the plasma as a function of axial distance. In addition, the total power transferred to the water cooling system can be calculated.

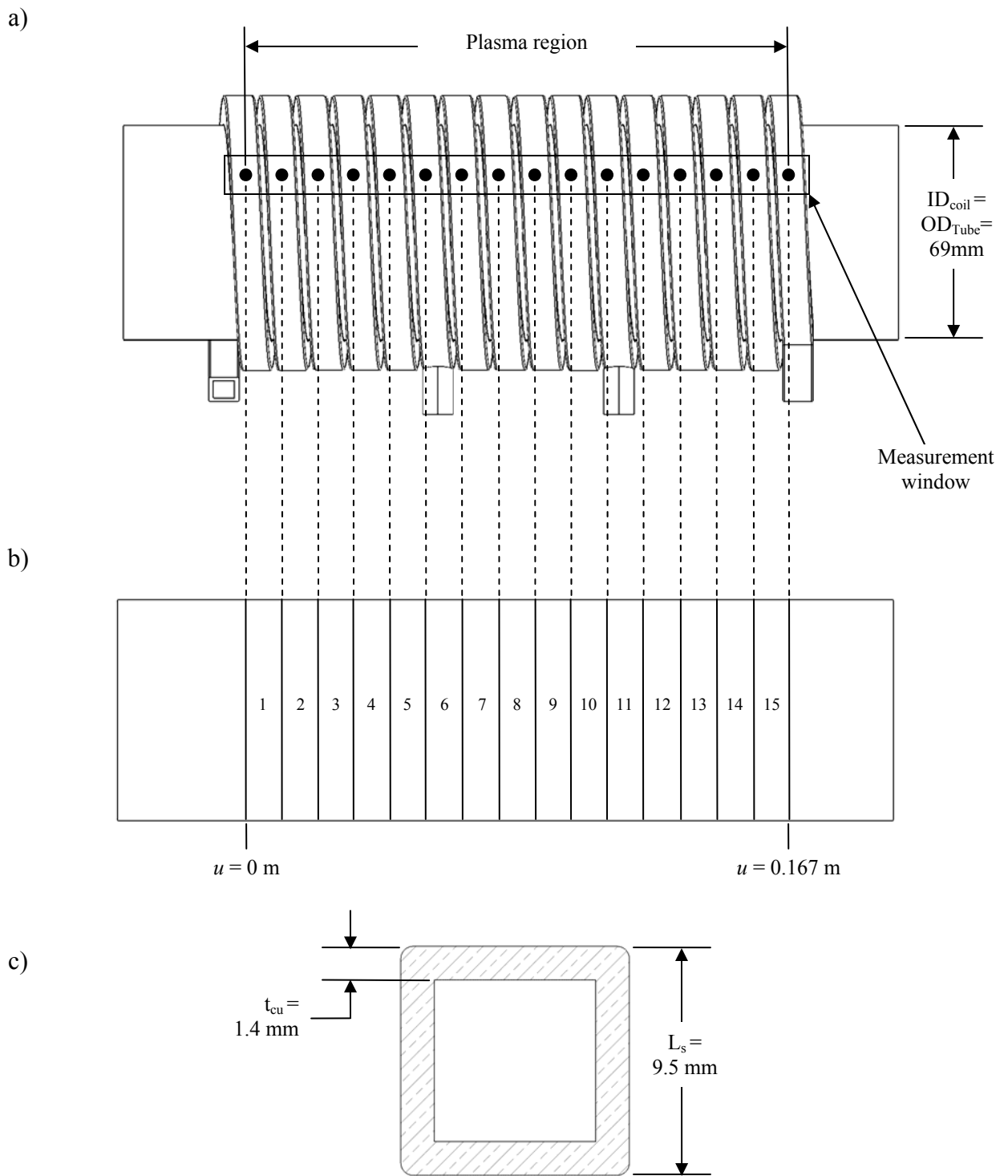


Figure 2.3 a) The black dots represent locations where thermal measurements are taken along the overall plasma region. b) The plasma region divided into 15 sections, each section is 11.1 mm wide. c) Cross-section of the coolant coil.

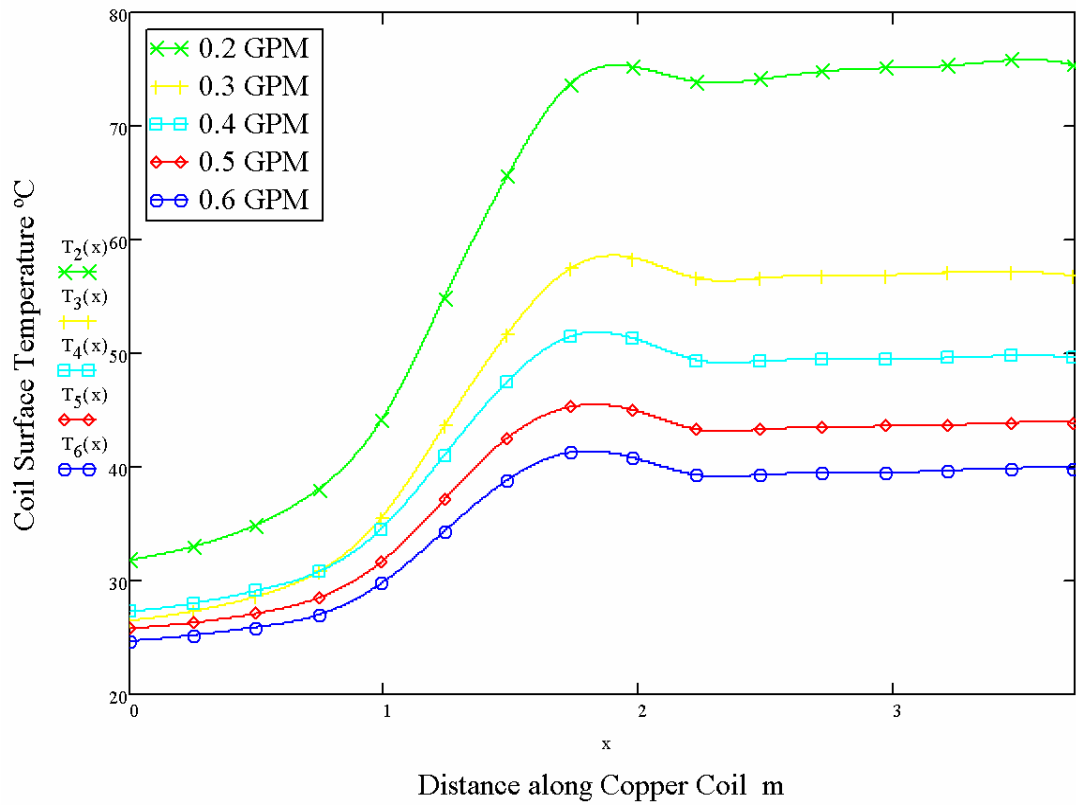


Figure 2.4 Measured surface temperatures as a function of distance along coolant coil at the locations shown in Figure 2.3 (a). The data are curve fit and shown for 0.2 -0.6 GPM flow rates.

2.3.a. Heat Flux Approximation Using Measured Coil Temperatures

(Method 1A)

The heat flux to the coils is given by the equation [Incropera and DeWitt, 1996]

$$q''(x) = h(T_w(x)) \cdot [T_s(x) - T_w(x)] \quad (2.2)$$

where $q''(x)$ is the heat flux in $\text{W}\cdot\text{m}^{-2}$, T_s is the coil surface temperature and T_w is the mean water temperature in $^{\circ}\text{C}$, both functions of the distance x along the coil. The heat transfer coefficient, h is in $\text{W}\cdot\text{m}^{-2}\cdot\text{K}^{-1}$ and is a function of $T_w(x)$ and many other parameters. For this expression, it is assumed that the temperature of the coolant coil is constant around the cross section. It is assumed that all energy from the plasma is convected to the water and losses to the ambient are negligible.

To calculate T_w , Equation 2.3 [Incropera and DeWitt, 1996] is used where P is the wetted perimeter in meters. This equation gives the water temperature for a differential element along the coil path knowing the surface temperature, again assuming that the coil has a homogenous temperature around the cross section at a given axial position. P , T_s and \dot{m} are known and all other variables are functions of T_w .

$$\frac{dT_w}{dx} = \frac{P}{\dot{m} \cdot C_p(T_w(x))} \cdot h(T_w(x)) \cdot [T_s(x) - T_w(x)] \quad (2.3)$$

To solve for T_w , the differential Equation 2.3 is solved with an initial water temperature guess equal to the incoming measured water temperature (although any initial temperature distribution could have been used). This procedure is repeated in an iterative fashion with the substitution of the most recently found water temperature profile. Convergence is determined when the residual is less than approximately 0.003. The iterative solution process was done for each flow rate, 0.2 GPM to 0.6 GPM. An example of a typical convergence history of $T_w(x)$ is plotted for the 0.2 GPM flow condition in Figure 2.5 (a), which shows that the final iterations do not change. The final water temperatures for the flow condition 0.2 GPM are plotted along with the coil temperature measurements in Figure 2.5 (b). It is noted that the temperature drop observed in the coil surface measurements at 2.2 meters is not present in the water temperature calculation. The water temperature profiles for each flow condition are shown in Figure 2.6.

The heat transfer coefficient, h , is calculated using the temperature curves in Figure 2.6. The coil is assumed to be a straight tube for these calculations. Equation 2.4 [Incropera and DeWitt, 1996] represents h

$$h(T(x)) = \frac{k(T(x)) \cdot Nu(T(x))}{D_h} \quad (2.4)$$

where h is in $\text{W} \cdot \text{m}^{-2} \cdot \text{K}^{-1}$, Nu is the dimensionless Nusselt number, k is the thermal conductivity of water in $\text{W} \cdot \text{m}^{-1} \cdot \text{K}^{-1}$ and D_h is the hydraulic diameter defined as

$$D_h = \frac{4 \cdot A_w}{P} \quad (2.5)$$

where A_w and P are the tube cross-sectional area in meters² and the wetted perimeter in meters, respectively.

The dimensionless Nusselt number can be calculated based on the knowledge of the flow physics and is defined in Equation 2.6. [Incropera and DeWitt, 1996] from a correlation from Gnielinski that was modified for $3000 < Re < 5 \times 10^6$.

$$Nu(T_w(x)) = \frac{\left(\frac{f(T_w(x))}{8}\right) \cdot (Re(T_w(x)) - 1000) \cdot Pr(T_w(x))}{1.0 + 12.7 \cdot \left(\frac{f(T_w(x))}{8}\right)^{\frac{1}{2}} \cdot \left(Pr(T_w(x))^{\frac{2}{3}} - 1\right)} \quad (2.6)$$

Re is the Reynolds number, Pr is the dimensionless Prandtl number, and f is the friction factor which is calculated from the Reynolds number for smooth tubes. First we calculate the Reynolds number using Equation 2.7 [Incropera and DeWitt, 1996] to verify that it is in the range required to use Equation 2.6.

$$Re(T_w(x)) = \frac{v_m \cdot D_h}{\nu(T_w(x))} \quad (2.7)$$

where v_m is the mean flow velocity in $m \cdot s^{-1}$ and ν is the kinematic viscosity in $m^2 \cdot s^{-1}$ as defined in Equation 2.1. The velocity is considered constant for each flow condition and the kinematic viscosity varies with T_w . The range for T_w in these experiments is approximately 25°C to 75°C so the Reynolds number will

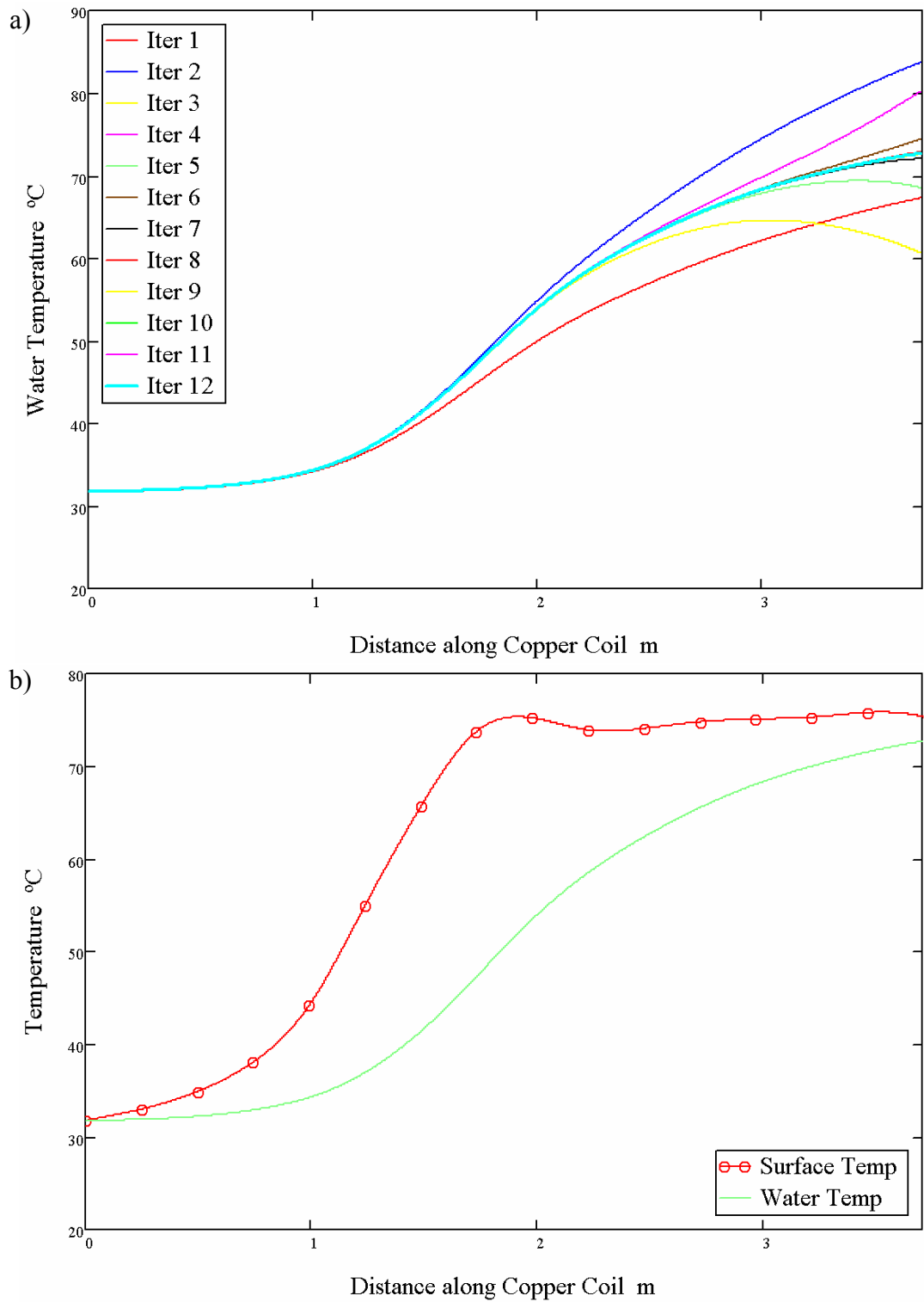


Figure 2.5 a) Example convergence history for each iteration at 0.2 GPM water flow rate, a total of twelve iterations calculated before convergence criteria met (0.003 °C residual). b) The final water temperature profile for the flow condition 0.2 GPM plotted with the coil surface temperature measurements.

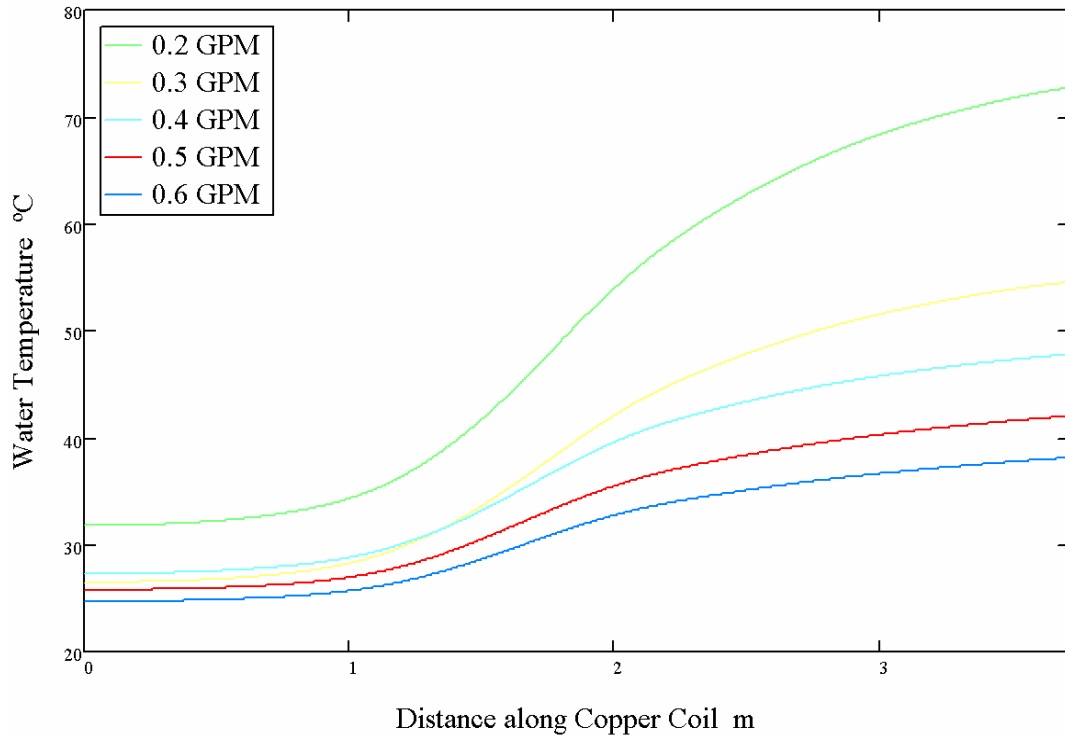


Figure 2.6 Final iterations for the water temperature calculations at each flow condition 0.2 – 0.6 GPM.

vary in the range $2100 < Re < 1.5 \times 10^4$. In low flow conditions, the Reynolds number is less than 3000 required for the use of Equation 2.6. Hence, for this analysis, the calculations are performed at higher flows where the Reynolds number is in the proper range. The Reynolds numbers are plotted as a function of water temperature for each of the flow conditions 0.2 – 0.6 GPM in Figure 2.7.

Next the Prandtl number, Pr is calculated from Equation 2.8 [Incropera and DeWitt, 1996] and plotted in Figure 2.8 as a function of T_w . The Prandtl number ranges from $2.4 < Pr < 6.1$ in the 25°C to 75°C temperature range.

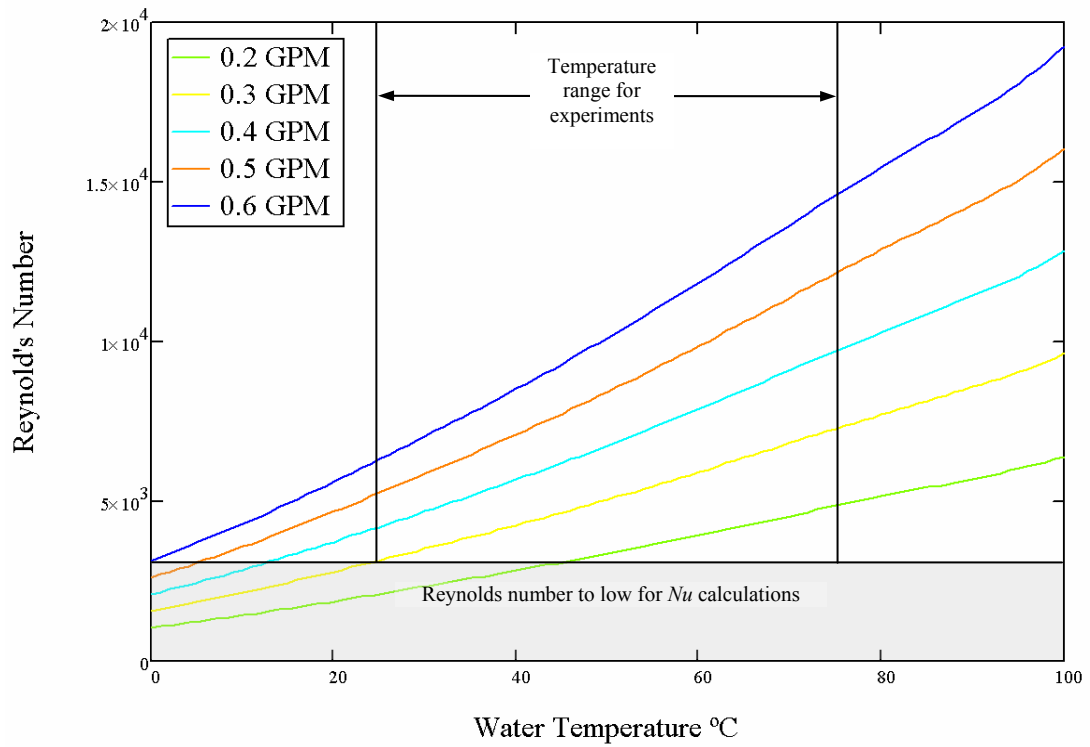


Figure 2.7 Reynolds number as a function of water temperature for each flow condition 0.2 – 0.6 GPM. The water temperature ranges from approximately 25°C to 75°C in these experiments.

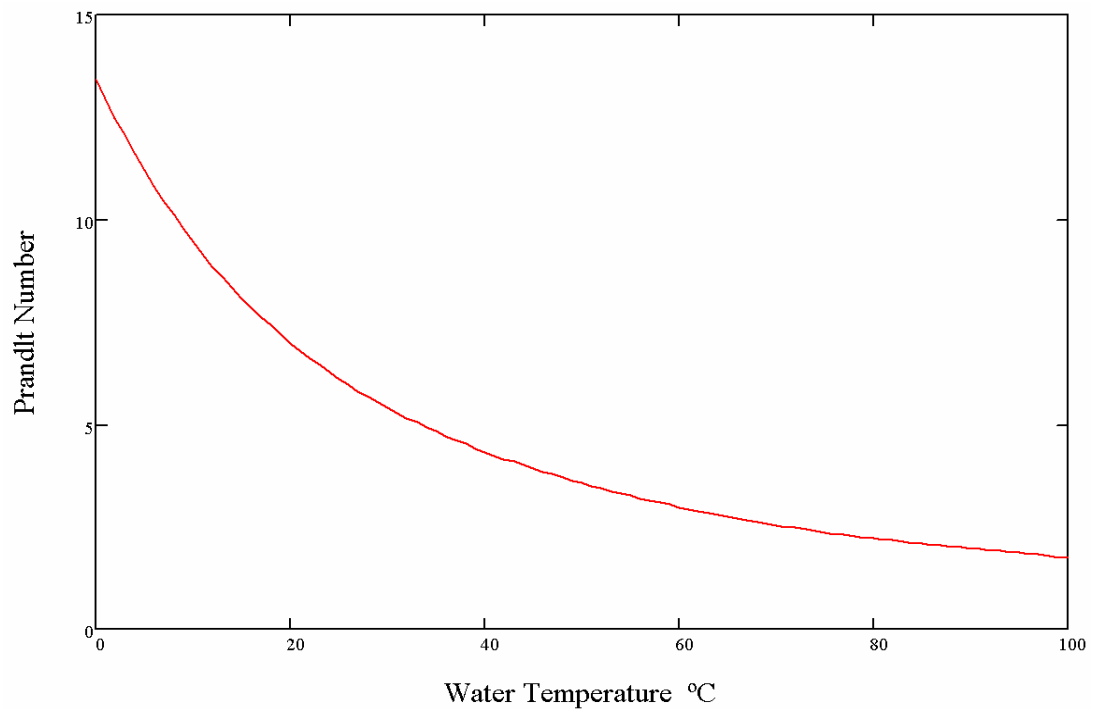


Figure 2.8 Prandtl number as a function of water temperature. The water temperature ranges from approximately 25°C to 75°C in these experiments.

$$\text{Pr}(T_w(x)) = \frac{C_p(T_w(x)) \cdot \eta(T_w(x))}{k(T_w(x))} \quad (2.8)$$

The friction factor is calculated from the Reynolds number and Equation 2.9 [Incropera and DeWitt, 1996] which is valid within the range $3000 < Re < 5 \times 10^6$ and is shown in Figure 2.9 for each of the flow conditions 0.2 – 0.6 GPM.

$$f(T_w(x)) = [0.79 \cdot \ln \text{Re}(T_w(x)) - 1.64]^{-2} \quad (2.9)$$

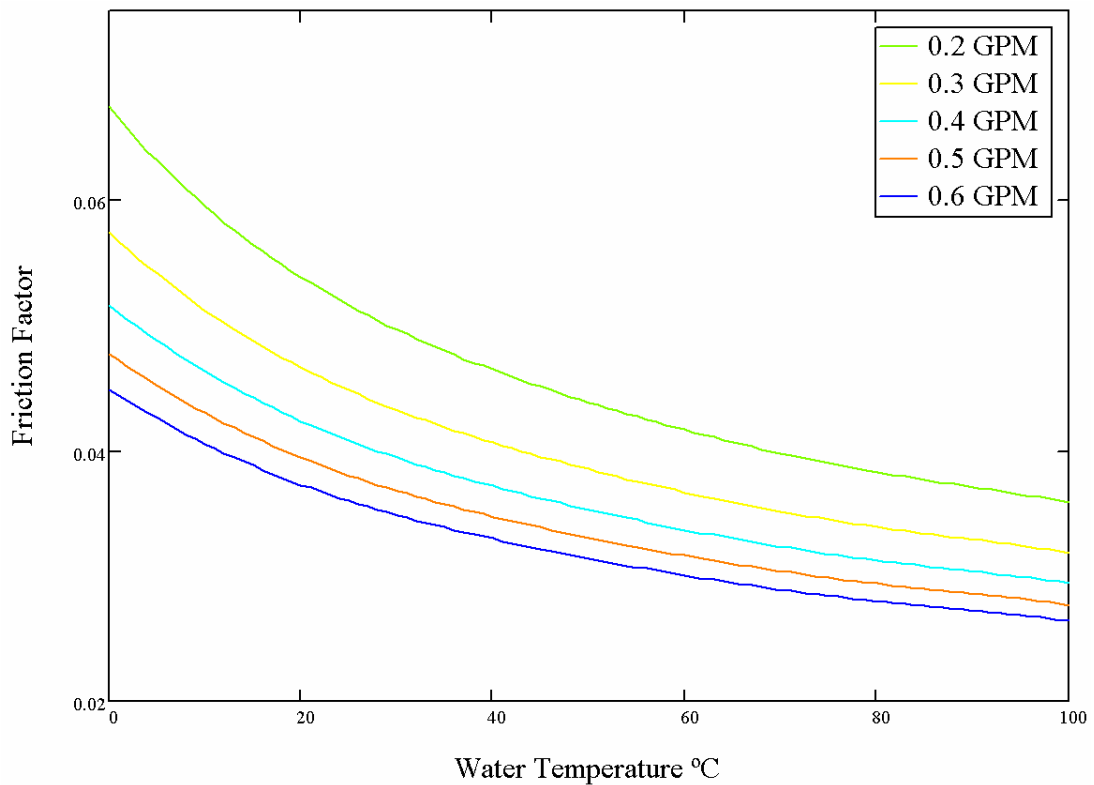


Figure 2.9 Friction factor as a function of water temperature for each flow condition 0.2 – 0.6 GPM. The water temperature ranges from approximately 25°C to 75°C in these experiments.

The heat flux to the internal chamber wall is calculated using Equation 2.2 and all of the parameters needed in Equation 2.2. The heat transfer coefficient is plotted as a function of water temperature for each of the flow conditions 0.2 – 0.6 GPM in Figure 2.10. Finally, the heat flux to the internal chamber wall is plotted as a function of distance u measured from the start of coil #1 in the plasma region for each of the flow conditions 0.2 – 0.6 GPM in Figure 2.11. Any secondary flow conditions caused by the helical coolant tube are neglected for these calculations since tube size is relatively small compared to the coil diameter (roughly 7:1).

As the flow rate increases, the heat flux calculations begin to agree with one another as expected. The curves nearly match from 0.5 - 0.6 GPM. To calculate the total power convected to the water each curve is integrated along the length of the coil and multiplied by the internal wetted perimeter of the coil. The total power convected to the water is 2124 ± 40 and 2114 ± 40 W for 0.5 and 0.6 GPM respectively. This is within the expected range of 2100 to 2400 W, assuming all power delivered into the plasma is transferred to the chamber wall. For verification, these values were also compared to those obtained using Equation 2.10 [Incropera and DeWitt, 1996] and the water temperatures calculated at the beginning of coil 1, T_{in} and the end of coil 15, T_{out} . This gives a gross power convected to the water (no spatial resolution) of 2120 ± 40 W for 0.5 GPM and 2110 ± 40 W for 0.6 GPM, both in agreement with the integrated result.

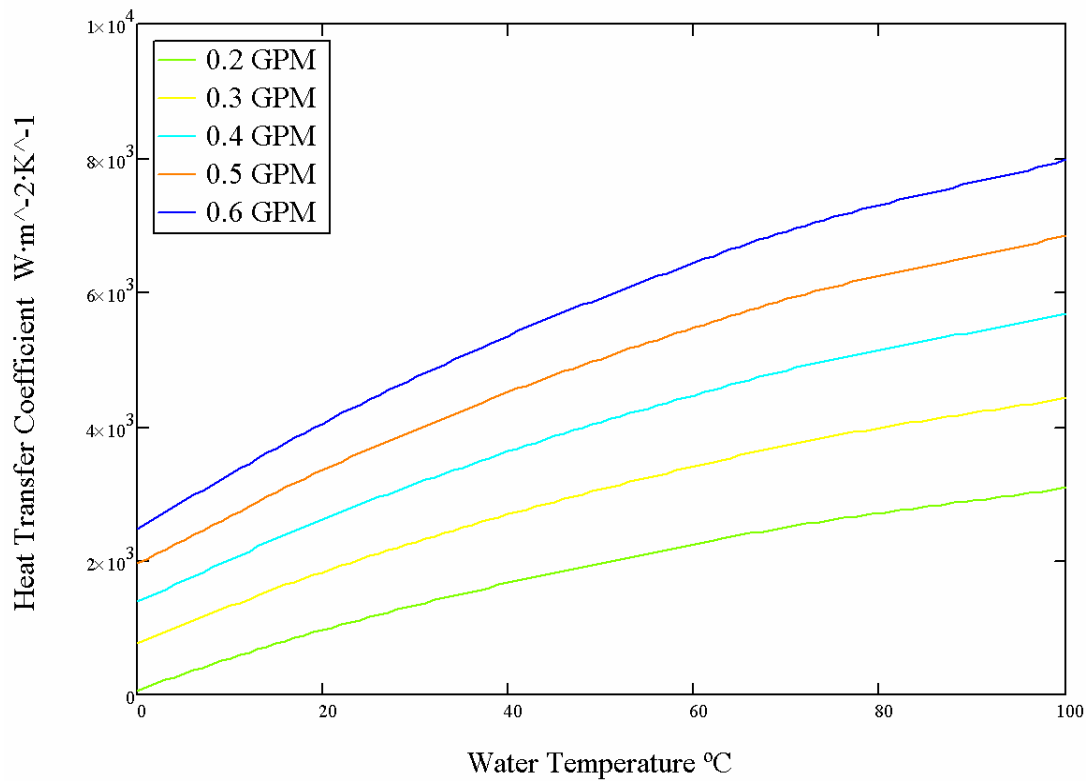


Figure 2.10 Heat transfer coefficient as a function of water temperature for each flow condition 0.2 – 0.6 GPM. The water temperature ranges from approximately 25°C to 75°C in these experiments.

$$Q(x) = \dot{m} \cdot C_p(T(x)) \cdot [T_{out} - T_{in}] \quad (2.10)$$

The calculations plotted in Figure 2.11 show that the heat flux distribution is nearly symmetric around the center of the coil, however, the tails of the heat flux curves are different. Although this non-symmetry could be attributed to capacitive coupling from the coil to the dissimilar grounded surfaces located at the two ends of the chamber, this effect is not expected to be so apparent at high powers, far from the transition between capacitive to inductive operation of the

coil that occurs at a few hundred watts. Another concern raised in Figure 2.11 is the variations observed between 0.2 - 0.4 GPM when compared to 0.5 and 0.6 GPM data. The plasma heat flux to the wall should be independent of the coolant flowrate. These concerns justify exploring one further step in refining the model developed to this point, which involves considering the temperature variations around the cross section of the coil.

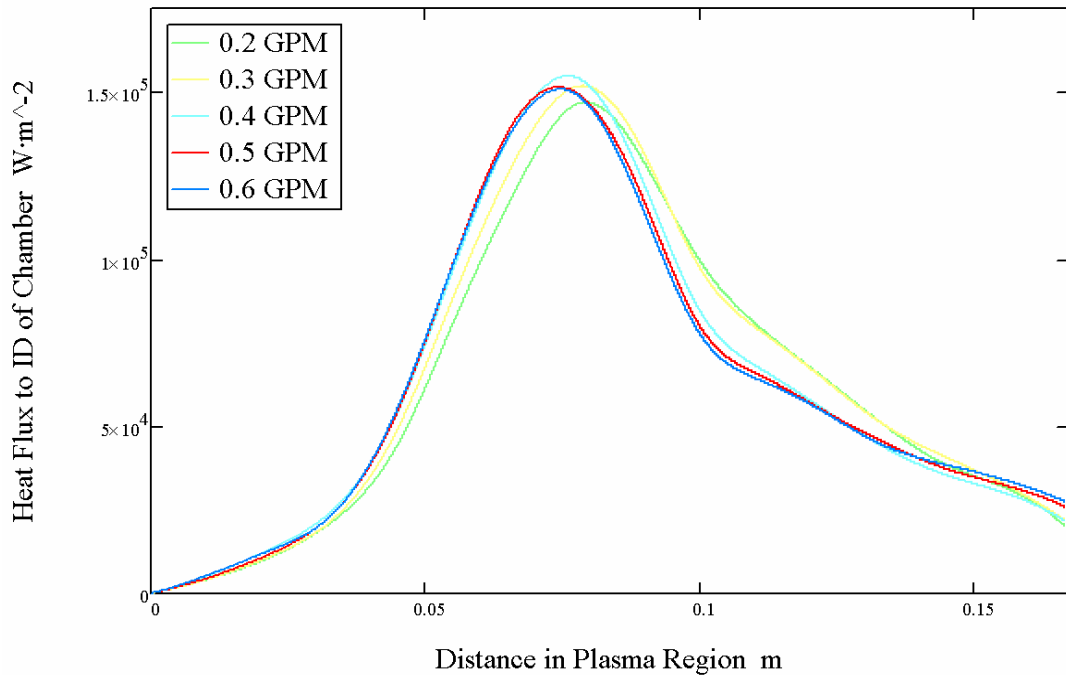


Figure 2.11 Heat flux to the internal surface of the chamber wall as a function of distance in the plasma region for flow conditions 0.2 – 0.6 GPM, Method 1A.

2.3.b. Heat Flux Approximation Including Effects of Temperature

Variation Around the Coil Cross-section (Method 1B)

The previous approximation in section 2.3.a. is a typical example of a heat transfer calculation. In this Section, the temperature around the coil cross-section is not assumed constant. This concept assumes a plasma power distribution and applies that to the inside (plasma side) of the coil to then calculate the resulting surface temperature of the coil at the points where they are measured. The power flux profile is manipulated until the calculated surface temperatures match the measured surface temperatures.

To begin, the coil cross-section is deconstructed and simplified as shown in Figure 2.12 (a). The hatched area is where the power calculation is performed. Since the coil is symmetric about the vertical axis, analysis only needs to be performed from $y = 0$ to $y = 2 \cdot L_s$ which is on the opposite side of the section from $y = 0$. Not by coincidence, $y = 2 \cdot L_s$ is where the temperature measurements are taken. Figure 2.12 (b) is the hatched area of 2.12 (a) straightened. The area is divided into two sections. Section 1 is located between $0 \leq y \leq L_s/2$ and is where the heat load Q_1 from the plasma reactor is applied. Section 2 has no heat load from the plasma and that surface (opposite the water) is assumed adiabatic. Both sections have heat load Q_2 that is convected to the water side of the coil. The surface temperature $T_s(y)$ is the coil temperature, assumed constant through the thickness. The mean water temperature is T_w . The x direction is in the length dimension of the coil as in the previous calculations. The coil thickness t_{cu} is also the same as before.

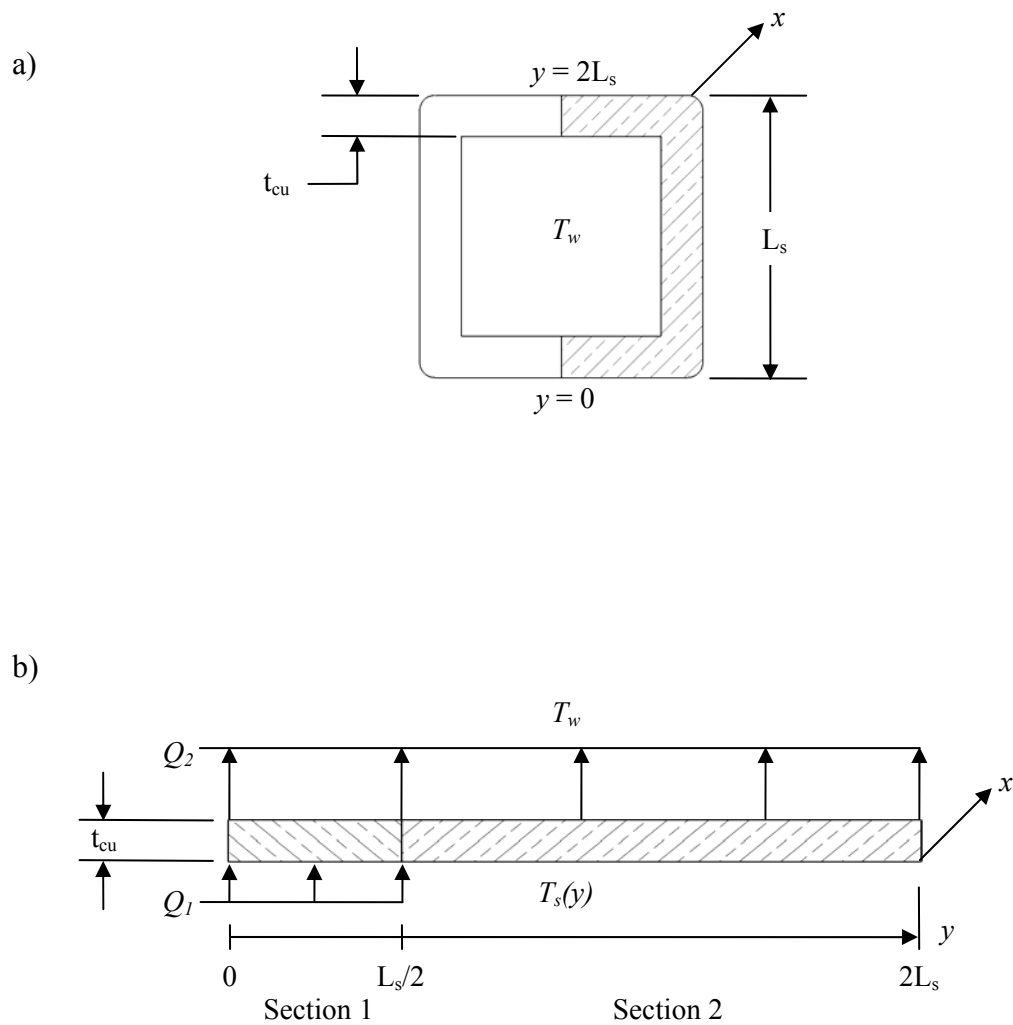


Figure 2.12 a) The coolant coil cross-sectional view. The hatched area is where the temperature calculations around the coil cross section are made. b) The hatched area in view a) made straight also showing heat loading to and from the coil surfaces. The area is divided into two sections, with and without heat load from the plasma reactor. All water side surfaces convect to the water.

To start the derivation, a power balance on a differential section of the coil dy is performed. The power balance is different for Section 1 and 2. $Q_1(y)$ is power from the plasma that is transferred to the coil, $Q_2(y)$ is the power convected to the water, and $Q_3(y)$ is the power conducted around the coil. Figure 2.13 contains diagrams showing the power balance in each section.

Beginning with Section 1, an equation can be written as follows from the energy balance on the differential section of the coil

$$dQ_1(y) + Q_3(y) = Q_3(y + dy) + dQ_2(y) \quad (2.12)$$

where $Q_3(y + dy)$ can be written as

$$Q_3(y + dy) = Q_3(y) + \frac{dQ_3(y)}{dy} dy \quad (2.13)$$

Substituting 2.13 into 2.12 yields

$$dQ_1(y) = dQ_2(y) + \frac{dQ_3(y)}{dy} dy \quad (2.14)$$

$dQ_1(y)$ is the power into the coil and can be written as

$$dQ_1(y) = x \cdot q''(y) dy \quad (2.15)$$

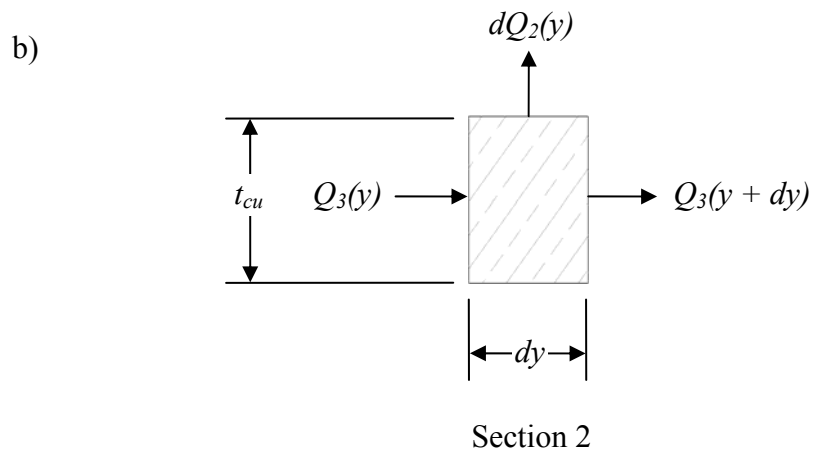
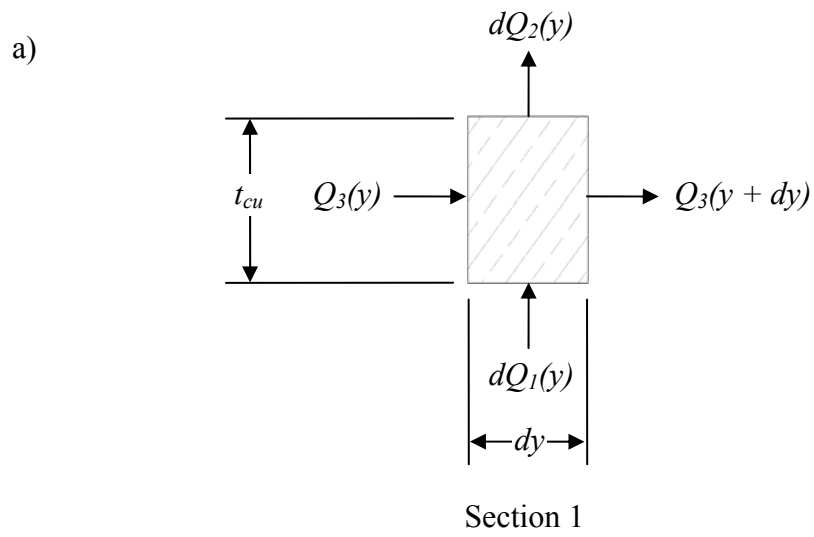


Figure 2.13 Power balance on a differential section of the coil dy for a) Section 1 and b) Section 2 representing the conditions stated in Figure 2.12.

where $q''(y) = \frac{Q_1(y)}{A}$ with $A = \frac{L_s}{2} \cdot x$ is the heat flux to the coil surface, and x is the length of one coil turn. $dQ_2(y)$ is the power convected to the water from the inside surface of the tube. This can be written using Equation 2.2 as

$$dQ_2(y) = h(T_w) \cdot x \cdot T(y) dy \quad (2.16)$$

where $T(y)$ is $T_s(y) - T_w$ and h is a function of T_w and is assumed constant for the differential element. $Q_3(y)$ is the conduction around the coil and can be written as

$$Q_3(y) = -k_{cu} \cdot x \cdot t_{cu} \cdot \frac{dT(y)}{dy} \quad (2.17)$$

which if differentiated is

$$\frac{dQ_3(y)}{dy} = -k_{cu} \cdot x \cdot t_{cu} \cdot \frac{d^2T(y)}{dy^2} \quad (2.18)$$

where k_{cu} is the thermal conductivity of copper in $\text{W} \cdot \text{m}^{-1} \cdot \text{K}^{-1}$. Substituting Equations 2.15, 2.16 and 2.18 into Equation 2.14 yields

$$x \cdot q''(y) dy = [x \cdot h(T_w) \cdot T(y) dy] - \left[x \cdot k_{cu} \cdot t_{cu} \cdot \frac{d^2T(y)}{dy^2} dy \right] \quad (2.19.a)$$

$$q''(y) - h(T_w) \cdot T(y) + \left[k_{cu} \cdot t_{cu} \cdot \frac{d^2 T(y)}{dy^2} \right] = 0 \quad (2.19.b)$$

$$\frac{q''(y)}{k_{cu} \cdot t_{cu}} - \left[\frac{h(T_w)}{k_{cu} \cdot t_{cu}} \cdot T(y) \right] + \frac{d^2 T(y)}{dy^2} = 0 \quad (2.19.c)$$

If Equation 2.19.a is set equal to zero the result is Equation 2.19.b and then if both sides are divided by $k_{cu} \cdot t_{cu}$ the final result is Equation 2.19.c. Now let

$x_0^2 = \frac{k_{cu} \cdot t_{cu}}{h(T_w)}$ and $T_0 = \frac{q''(y)}{k_{cu} \cdot t_{cu}}$ then the result is differential Equation 2.20 with a

solution Equation 2.21.

$$\frac{d^2 T(y)}{dy^2} - \frac{T(y)}{x_0^2} + T_0 = 0 \quad (2.20)$$

$$T_1(y) = c_1 \cdot e^{\frac{+y}{x_0}} + c_2 \cdot e^{\frac{-y}{x_0}} + T_0 \cdot x_0^2 \quad (2.21)$$

Equation 2.21 is the temperature drop around the coil in Section 1. The constants c_1 and c_2 will be calculated later.

This same process is used to develop the temperature equation in Section 2 of the coil and the resulting differential equation is

$$\frac{d^2T(y)}{dy^2} - \frac{T(y)}{x_0^2} = 0 \quad (2.22)$$

with a solution of the form

$$T_2(y) = c_3 \cdot e^{\frac{+y}{x_0}} + c_4 \cdot e^{\frac{-y}{x_0}} \quad (2.23)$$

Equation 2.23 is the temperature drop around the coil in Section 2 of the coil cross-section.

The constants c_1 , c_2 , c_3 and c_4 can be calculated by applying boundary conditions to Equations 2.21 and 2.23. The boundary conditions follow as

$$\left. \frac{dT_1(y)}{dy} \right|_{y=0} = 0$$

and

$$\left. \frac{dT_2(y)}{dy} \right|_{y=2 \cdot L_s} = 0$$

which set up the conditions for Equations 2.24.a and 2.24.b.

There is one other unique position at $y=L_s/2$ where the energy Q_l ceases and is the boundary between the temperature in Section 1, T_1 and the temperature in Section 2, T_2 . This sets up two conditions. First, the slopes on either side of $y=L_s/2$ are different since the left side has additional power that the right side does not, however, the slopes must be equal at this position to avoid an infinite power

density. These two conditions allow one to solve for the remaining constants using equations 2.24.c and 2.24.d. These four equations allow us to find the values for the four unknown constants.

$$\left. \frac{dT_1(y)}{dy} \right|_{y=0} = 0 = \frac{c_1}{x_0} - \frac{c_2}{x_0} \quad (2.24.a)$$

$$\left. \frac{dT_2(y)}{dy} \right|_{y=2 \cdot L_s} = 0 = \frac{c_3}{x_0} \cdot e^{\frac{2 \cdot L_s}{x_0}} - \frac{c_4}{x_0} \cdot e^{-\frac{2 \cdot L_s}{x_0}} \quad (2.24.b)$$

$$\left. \frac{dT_1(y)}{dy} \right|_{y=\frac{L_s}{2}} = \left. \frac{dT_2(y)}{dy} \right|_{y=\frac{L_s}{2}} = \frac{c_1}{x_0} \cdot e^{\frac{L_s}{2 \cdot x_0}} - \frac{c_2}{x_0} \cdot e^{-\frac{L_s}{2 \cdot x_0}} = \frac{c_3}{x_0} \cdot e^{\frac{L_s}{2 \cdot x_0}} - \frac{c_4}{x_0} \cdot e^{-\frac{L_s}{2 \cdot x_0}} \quad (2.24.c)$$

$$T_1(y) \Big|_{y=\frac{L_s}{2}} = T_2(y) \Big|_{y=\frac{L_s}{2}} = c_1 \cdot e^{\frac{L_s}{2 \cdot x_0}} - c_2 \cdot e^{-\frac{L_s}{2 \cdot x_0}} + T_0 \cdot x_0^2 = c_3 \cdot e^{\frac{L_s}{2 \cdot x_0}} - c_4 \cdot e^{-\frac{L_s}{2 \cdot x_0}} \quad (2.24.d)$$

The final solution is the result of an iterated power profile that when applied to Section 1 as Q_I , yields the measured surface temperature

$$T_s = T_2(2 \cdot L_s) + T_w \quad (2.25)$$

To accomplish this, a heat flux to the ID of the chamber is assumed at a distance, x , along the coil. This is used to calculate T_0 and in turn, the temperature at $T_2(2L_s)$. The water temperature T_w can be calculated using Equation 2.10 where T_{in} is the water temperature at $x = 0$ (the initial water temperature) and T_{out} is the water temperature at distance x along the coil. The total power input into the water is calculated by integrating from 0 to x in the plasma region and multiplying by the internal perimeter of the reactor dielectric. Once T_w is calculated, then the surface temperature, T_s is known from Equation 2.25. This process is performed at 8 equally spaced points along the tube and curve fit to obtain a function where the heat flux can be calculated at any distance along the coil scaled to the plasma region (shown in Figure 2.14 for each of the flow conditions 0.2 – 0.6 GPM). As the flow rate increases, the heat flux calculations converge. The curves nearly match from 0.4 - 0.6 GPM. The total power convected to the chamber is 2332 ± 40 and 2342 ± 40 W for 0.5 and 0.6 GPM respectively and is within the expected range of 2100 to 2400 W, assuming all power input into the plasma is transferred to the dielectric wall. Once again, these values were also compared to the gross calculations obtained by using Equation 2.10 and the water temperatures calculated in this section at the beginning of coil 1 and the end of coil 15. This

gives a gross power convected to the water (no spatial resolution) of 2327 ± 40 W for 0.5 GPM flow data and 2334 ± 40 W for 0.6 GPM flow data, both in good agreement with the integrated result.

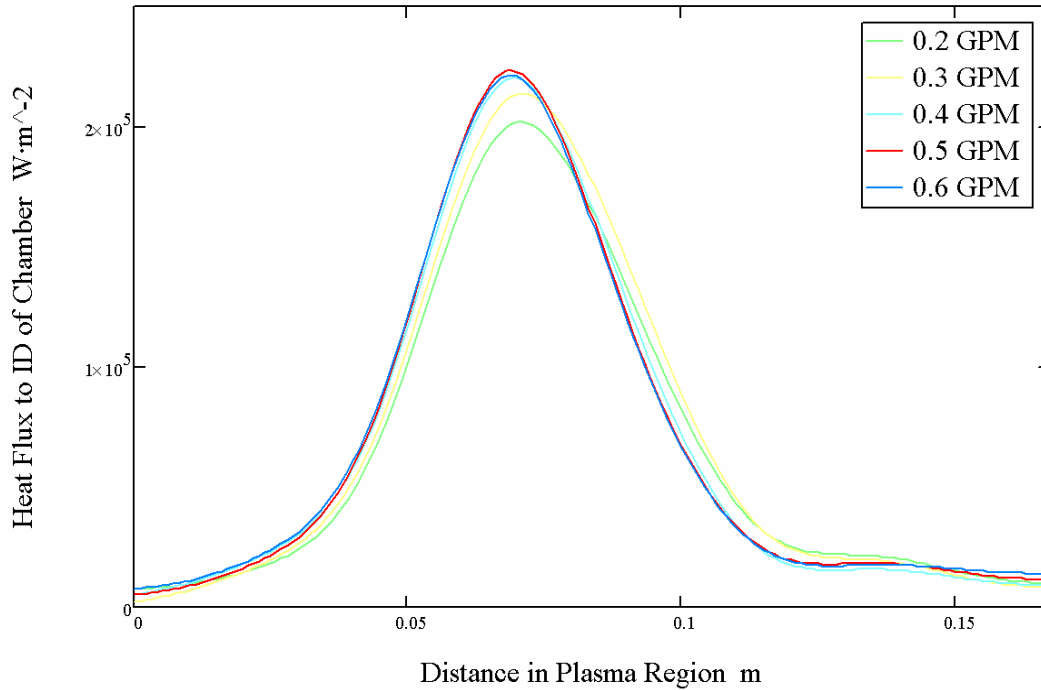


Figure 2.14 Heat flux to the internal surface of the chamber wall as a function of distance in the plasma region for each flow condition 0.2 – 0.6 GPM, Method 1B.

It is interesting to note the significant temperature change around the coil cross-section in the area of high heat flux at the peak of the curve in Figure 2.14 which is illustrated in Figure 2.15.

The spatially resolved heat flux shows a more symmetrical distribution when compared to the results in Figure 2.11 where the assumption of a constant

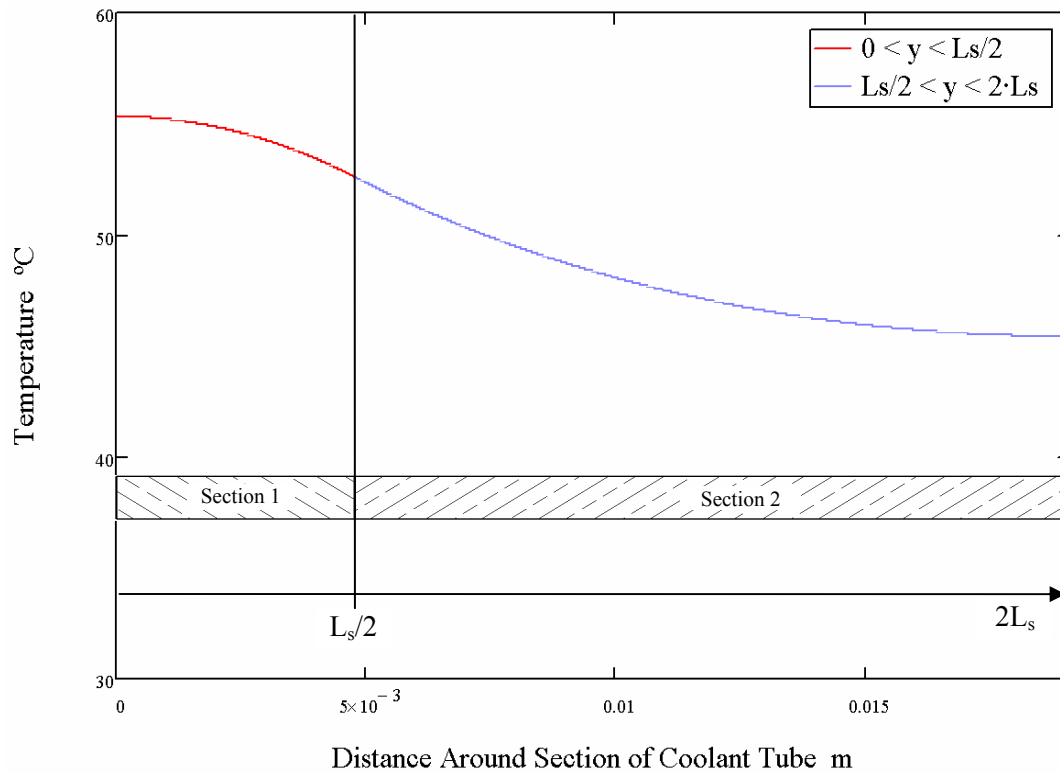


Figure 2.15 Significant temperature change around the coil cross-section in the area of high heat flux at the peak of the curve in Figure 2.14.

temperature around the coil cross section was made. The next Section expands upon the model using CFD techniques to account for the dependence between water and tube temperatures, water properties and heat load distribution from this section are applied to the coil. The CFD simulation will also be used to both validate the spatially resolved heat load profiles obtained from the analytical model and improve the accuracy of the heat load profile.

2.4. Conjugate Heat Transfer CFD Simulation

To gain a better understanding of the water dynamics and temperature property distribution and the effects on the surface temperature of the coil, a computational fluid dynamics simulation was developed. The model simulates the same 15-turn helical coil using the ANSYS® CFX CFD software package.

As with all simulations, the mesh is arguably the most critical part of the model. A mesh independence study was performed on a simpler 2-turn coil to verify convergence of the results as the mesh was refined. When these meshing data were applied to the 15-turn coil, it became too computationally intensive and a slightly less optimal mesh was selected as a compromise. The less optimal mesh will still provide good insight into the physics of the problem but with less accuracy. The water volume utilizes a mesh “inflation” technique that puts more elements in the boundary layer at the solid-fluid interface and is illustrated in a section view shown in Figure 2.16.

Standard boundary conditions are used for this model. The heat load calculated by Method 1B is applied to the inside surface of the coil and the water flow is 0.6 GPM. All other external surfaces are adiabatic. The internal surfaces of the tube are assumed smooth with no slip and the initial water temperature is 25°C at the inlet. The material properties for water and copper at standard conditions are included with the software and used when programming the simulation.

After the simulation reached good convergence, these data were transferred to the post processor where they could be visualized. Images of the

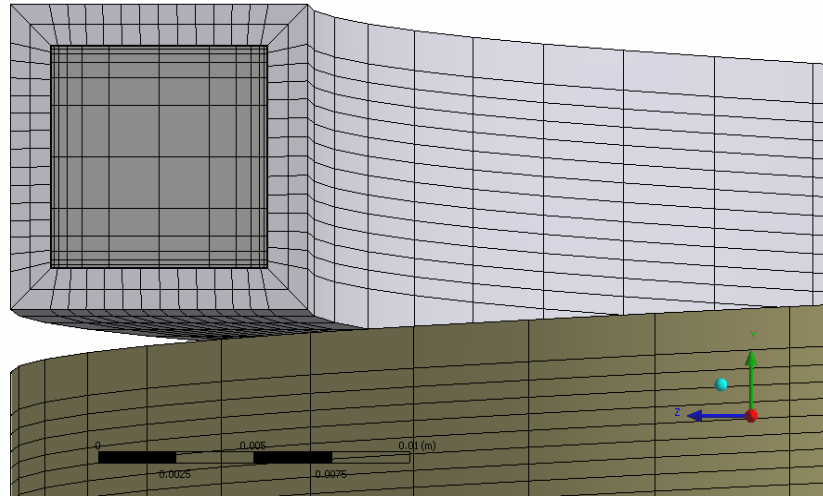


Figure 2.16 View of the final mesh used for the CFD 15 coil simulation.

temperature results from the simulation were captured and are depicted in Figure 2.17 as section views. Figure 2.17 (a) depicts the temperatures of the coil and Figure 2.17 (b) shows the water temperatures. These figures show a section of the coil, near the center where the majority of the heat is deposited, that do not have uniform coil or water temperatures through the cross section. The coil surface temperatures in this region (where the measurements are taken) are higher than the average water temperature due to heat conduction around the tube and non-uniform water temperature in the bulk. As the heat flux is reduced, the water temperature difference becomes more uniform and the coil surface temperature is reduced. Referring back to the measured temperature data in Figure 2.4, the

surface temperature reduction of the coil does not represent heat loss from the region. Rather, it shows a misleading surface temperature caused by heat conduction around the coil cross section and non-uniform water temperature in the bulk. Figure 2.17 also nicely illustrates the complexity of the heat transfer problem solved.

Temperatures taken from the model at the outer surface of the coil in the same locations as the experimental data are plotted along with the experimental data at 0.6 GPM in Figure 2.18. The simulation agrees very well with the measured results, and shows that the analytical model is very good for predicting the spatial distribution of the heat load.

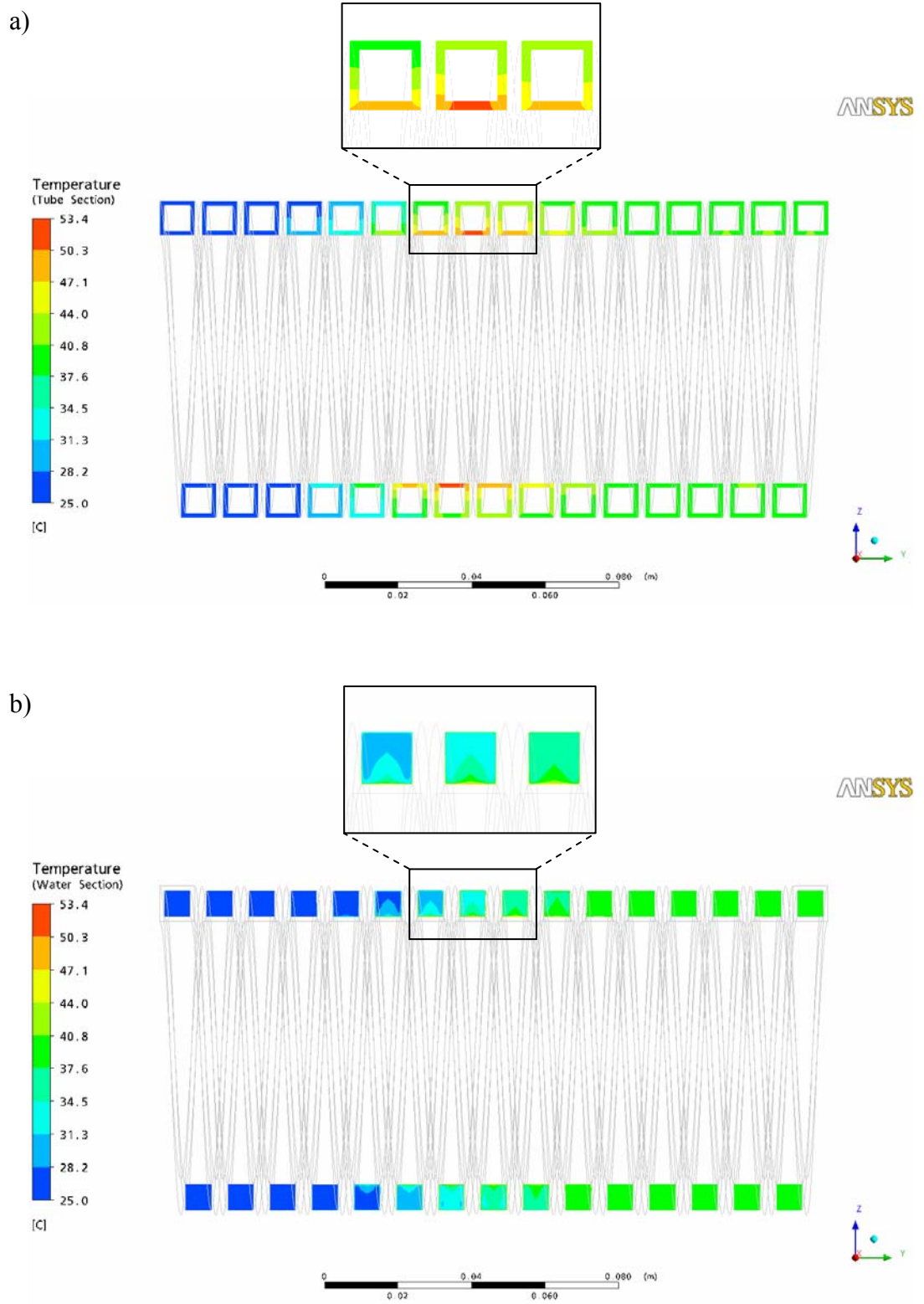


Figure 2.17 CFD simulation of the 15-turn coolant coil. The heat load calculated from Method 1B is applied to the inside surface of the coil and water flowrate is simulated at 0.6 GPM and 25°C.
 a) Section view of the coil. b) Section view of the water.

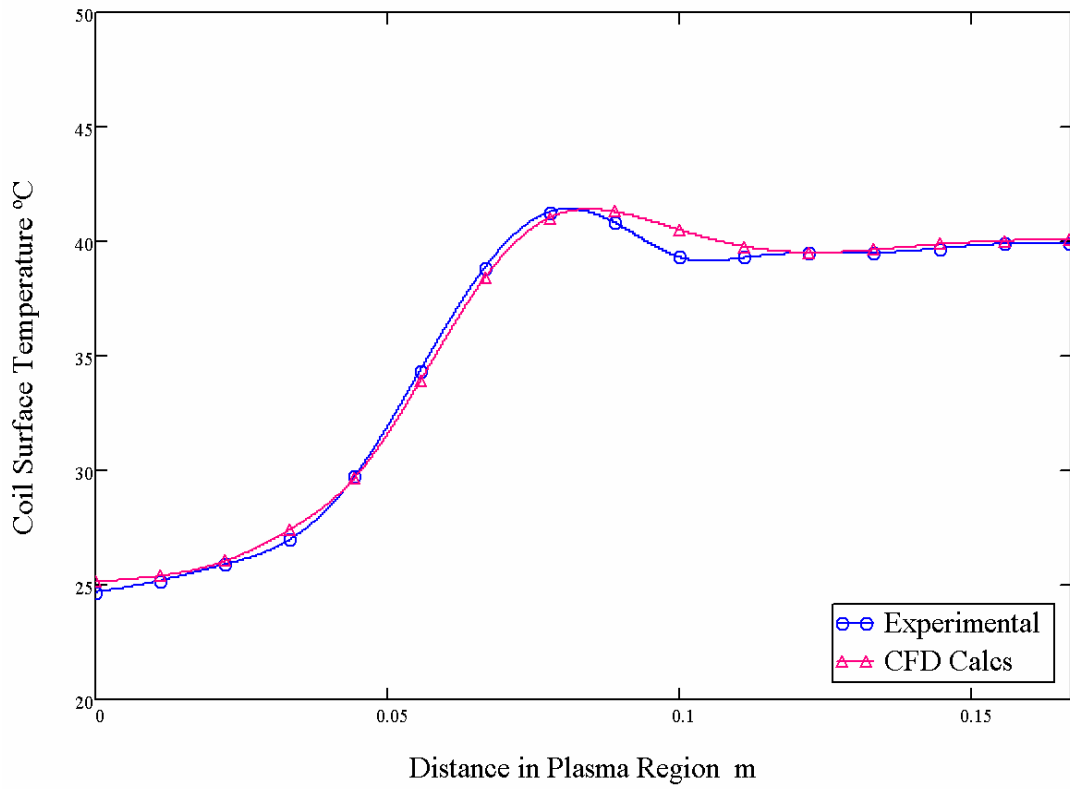


Figure 2.17 Measured coolant coil surface temperatures plotted with the surface temperature calculations from the CFD simulation. Heat loads calculated from Method 1B were applied to the CFD model and the water flow rate is 0.6 GPM for both curves.

2.5. Conclusions

This chapter describes the first of two methods used to determine the spatial heat flux to the internal wall of a cylindrical ICP reactor. This method uses the rise in coolant temperature circulating through the cooling system of a plasma chamber to spatially estimate the power deposited on the chamber walls. Although the applicability of the method is not limited by the material properties of the dielectric, it is better suited for reactors that have (1) very good thermal coupling to the coolant and (2) a high density of coolant tubing in contact with the dielectric.

The analytical method presented here is shown to provide good agreement with both independent determinations of the total deposited power, and the results of spatially resolved calculations using Computational Fluid Dynamics (CFD).

REFERENCES

- Munson, Young and Okiishi (1990), "Fundamentals of Fluid Mechanics",
John Wiley & Sons, Inc.
- Incropera and DeWitt (1996), "Fundamentals of Heat and Mass Transfer",
John Wiley & Sons, Inc.

CHAPTER 3

HEAT FLUX TO THE DIELECTRIC CHAMBER MATERIAL DETERMINED BY CALORIMETRY OF DIELECTRIC TEMPERATURE

3.1 Introduction

The previous Section described an analytical method that allows determining the spatially resolved heat load from measurements of the temperature rise in a cooling fluid. Although the method shows agreement with independent determinations of the heat load, its applicability is somewhat limited to cases where the cooling circuit and the chamber wall are in close thermal contact. Alternatively, the heat flux to the inner surface of the plasma reactor can be determined by measuring the temporal response of a reactor to a suddenly applied plasma heat load and comparing the response to a thermal capacitance model of the dielectric chamber material. In this case, however, there should be poor thermal contact between the coolant tubing and the reactor chamber and the dielectric chamber should be selected to have very poor thermal conductivity. This approach will be referred to as Method 2. Changes in time of the bulk temperature along with desirable material properties of the dielectric will make it possible to calculate the power profile applied to the volume in the plasma region. For the model to provide correct results there can not be significant uncontrolled cooling of the dielectric tube or significant heat spreading along the tube axially. As stated earlier, the remote plasma source being evaluated is available with two different chamber material options, alumina and quartz. The quartz material is

chosen for the temporal study because of its very poor thermal conductivity, $1.35 \text{ W}\cdot\text{m}^{-1}\cdot\text{K}^{-1}$, relative to Alumina, $38.9 \text{ W}\cdot\text{m}^{-1}\cdot\text{K}^{-1}$. The density and specific heat of Alumina and quartz are similar and so the low conductivity quartz minimizes the heat spreading that occurs down the length of the tube, which would otherwise smear out features of the heat flux profile. Since the current reactor used in the previous section has the coolant tubing encapsulated to the chamber tube, it can not be used here. Instead, a new reactor is made with modifications, but with the same inductive coupling and plasma generation geometry.

3.2 Experimental Setup

The plasma reactor for this study has a dielectric chamber that is 2 mm smaller in diameter compared to the original reactor (OD = 67 mm instead of 69 mm). The change in diameter was necessary to minimize thermal contact between the chamber and coil. The assembly is not encapsulated with conductive material and is therefore not actively cooled. All other aspects of the new reactor are identical to the encapsulated coil reactor. Refer to Figure 3.1 for an illustration. Similar to the previous experiment, calculations are performed

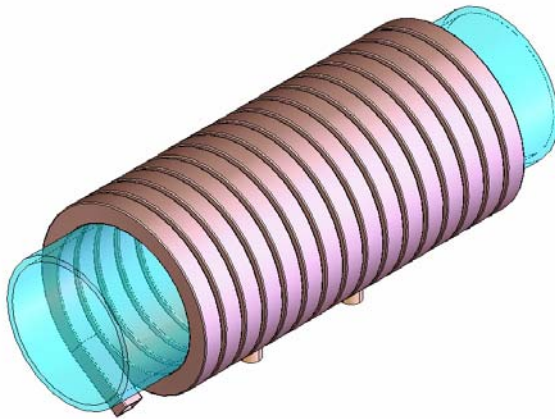


Figure 3.1 The new reactor design in isometric view. There is no encapsulant surrounding the quartz tube so the coolant coil is not in good thermal contact with the dielectric.

on 15 equal segments of the reactor in the plasma region and are used to estimate heat flux to the plasma facing wall. In this experiment, the surface temperatures of the dielectric are measured between the turns of the copper coil (instead of on

the coil turns as before) using the same infrared camera technique. The chamber is painted with a high emissivity opaque material to ensure good thermal readings and prevent the optical emissions of the reactor plasma from affecting the readings. Figure 3.2 shows the locations of the temperature measurements. The measurements are made in the same area of the reactor as before. The thermal capacitance model uses the change in bulk temperature of the dielectric material over a given amount of time to estimate the power being applied. In this case, the temperature difference is calculated for a given amount of plasma ON time and after the volume of the dielectric wall becomes uniform in temperature through the thickness. Figure 3.3 shows a typical thermal image of the reactor after 5 seconds of plasma ON. It is noted that the chamber started with a uniform ambient temperature of 25°C for this test.

One consideration in this technique that was not of concern using Method 1 in Chapter 2 is the placement of the thermal camera in relation to the points of measurement. In Method 1, the temperature readings were from the easy-to-view external surface of the coolant coil, but for Method 2, the temperature readings are at the surface of the quartz tube are made in a cavity created by the copper coil. The amount of radiation the camera aperture receives can be shadowed by the vertical walls of the coil, which could reduce the temperature reading by the camera. The copper material is a good reflector of this radiation, reducing the severity of the problem, but, for worst case conditions, the reflection is ignored and simple geometry is used to determine the percentage of radiation that will make it to the camera. Figure 3.4 shows this geometry for a few coil sections.

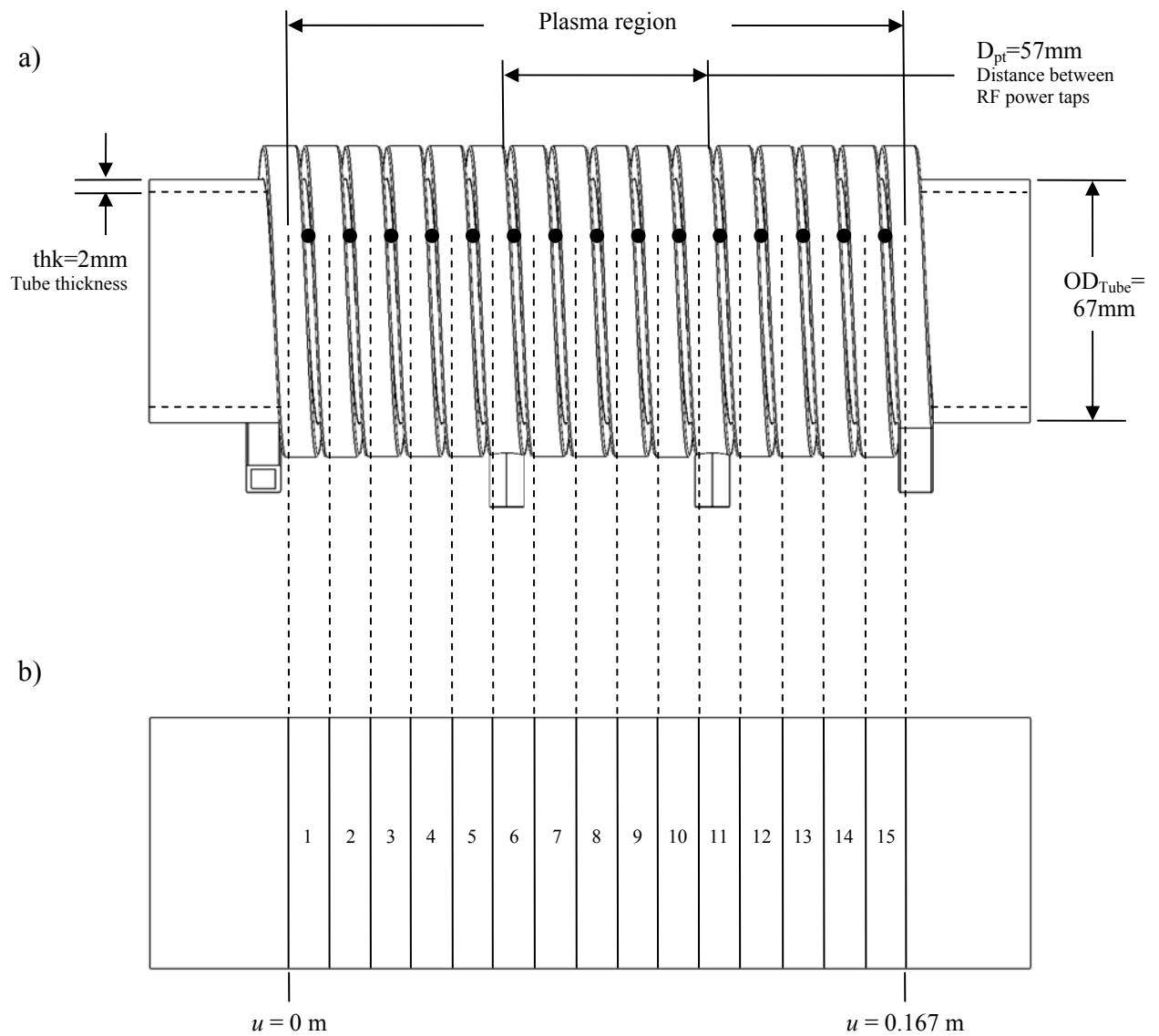


Figure 3.2 a) The black dots represent locations where thermal measurements are taken. b) The plasma region is divided into 15 sections, each section is 11.1 mm wide.

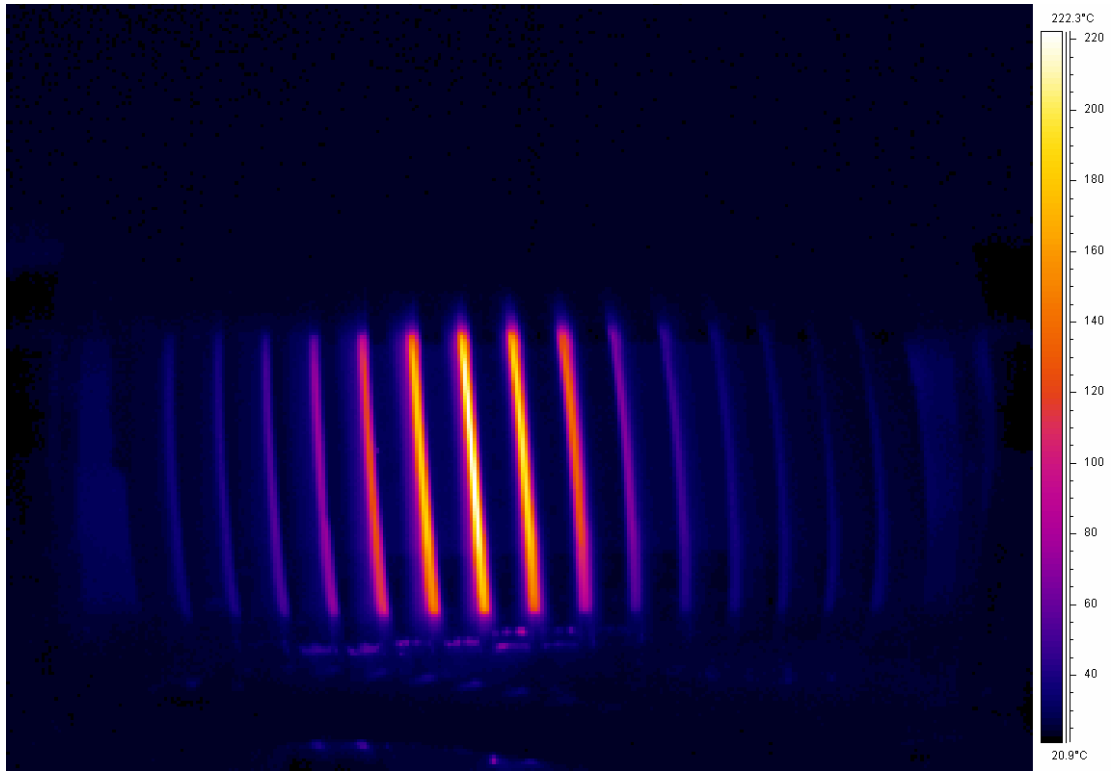


Figure 3.3. A typical thermal image of the source after 5 seconds of plasma ON time.

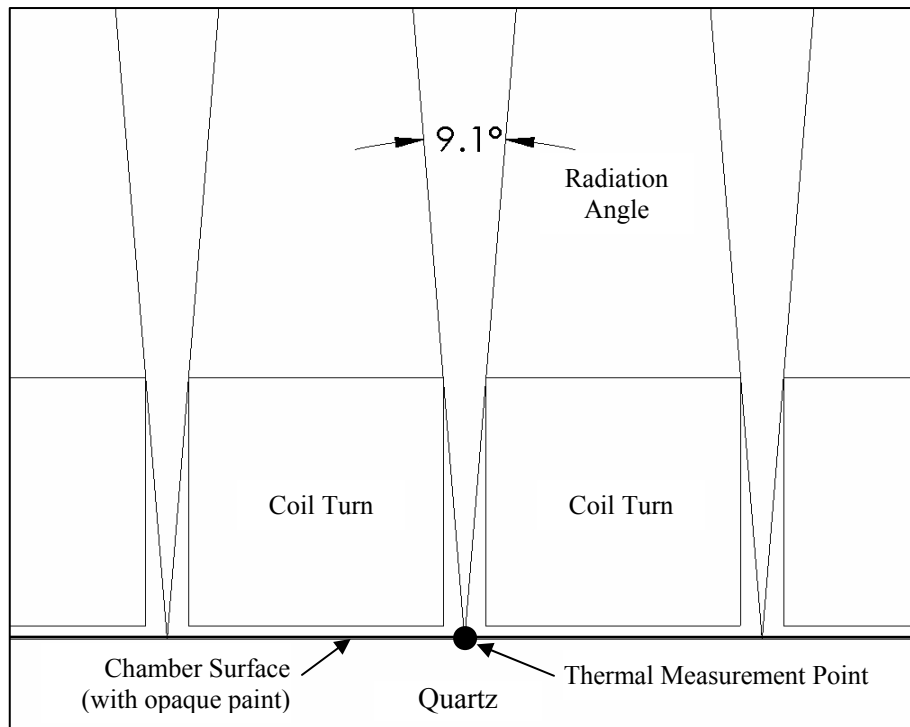


Figure 3.4 Geometry of dielectric chamber wall and coils where a 9.1° viewing angle exists over which thermal radiation will leave the chamber surface (ignoring reflections from the coolant coil turns). This will determine the amount of radiation seen by the camera for each thermal measurement location.

The measurement points are assumed to be centered between the coils. There is a 9.1° angle created from that point to the corners of the coil. The camera aperture diameter is 47 mm and is located 0.673 meters from the surface of the quartz tube. The effect of the projection of the thermal measurement points onto the camera aperture is shown in Figure 3.5 as a plot of the percent of radiation for each measurement point that is projected to the camera as a function of distance. The majority of the plasma power is deposited in the region where the camera sees 100% of the radiation. The camera could be placed further from the tube to

improve the visibility, however, the resolution of the image will suffer. The current distance of 0.673 m was selected as a compromise of acceptable image resolution and thermal results.

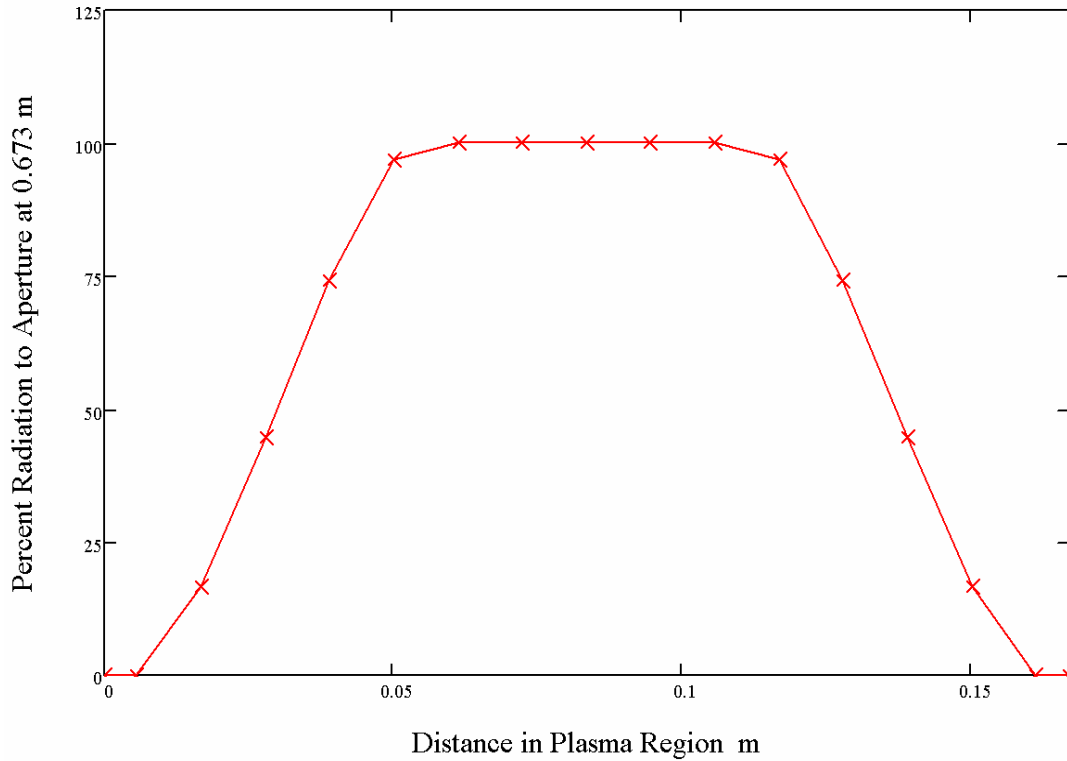


Figure 3.5 The percent of radiation that makes it to the camera aperture for each measurement point along the plasma region. The aperture is centered in the plasma region located 0.673 m for the surface of the reactor chamber.

3.3 Calculation of Heat Flux Based on Dielectric Wall Temperature Rise

The power to each of the 15 sections can be calculated using a thermal capacitance model. This model assumes a uniform temperature in each section and that the net energy stored in the volume, after a certain time, is equal to the total energy transferred to the volume minus the energy loss from the volume. Equation 3.1 represents this conservation of energy

$$E_{net} = E_{in} - E_{out} \quad (3.1)$$

where E_{net} is the measure net energy stored in the volume, E_{in} is the total energy transferred to the volume, and E_{out} is the energy transferred out of the volume, all in Joules.

There are two important parameters to calculate when determining whether or not a transient thermal capacitance model will be accurate. These are the Biot number and Fourier number. The Biot number is the ratio of resistance of conduction in the solid to the energy loss from the surfaces of the solid to the surroundings. The Fourier number is a dimensionless time that represents a measure of the relative effectiveness with which a solid conducts and stores thermal energy. These two numbers together help determine the legitimacy of the transient thermal model being invoked herein and are defined in Equation 3.3 and 3.4 [Incropera and DeWitt, 1996]

$$Fo = \frac{k_{SiO_2}}{\rho_{SiO_2} \cdot Cp_{SiO_2}(T(t))} \cdot \frac{t}{L_c^2} \quad (3.3)$$

$$Bi = \frac{h(T(t)) \cdot L_c}{k_{SiO_2}} \quad (3.4)$$

where k_{SiO_2} is the thermal conductivity of quartz, Cp_{SiO_2} is the heat capacitance for quartz in $J \cdot Kg^{-1} \cdot ^\circ C^{-1}$ (a function of the bulk temperature), ρ_{SiO_2} is the density in $Kg \cdot m^{-3}$, h is the heat transfer coefficient from the surface to the surroundings in $W \cdot m^{-2} \cdot ^\circ C^{-1}$ and the characteristic length is $L_c = \frac{V}{A_s}$ in meters. The heat capacitance for quartz changes with temperature significantly and is shown in Appendix B. This effect is taken into account for each section since there is a significant difference in temperature among the 15 sections. The density and thermal conductivity do not change much in this temperature range and are considered constant.

The Fourier number is considered for two different scenarios, the radial direction, Fo_r and the u direction, Fo_u . The difference between the two being the characteristic length $L_c = thk$ (tube thickness) in the radial direction and $L_c = D_{pt}$ (distance between power taps where the majority of power is applied) in the u direction. Refer to Figure 3.2 (a) for details of that geometry. It is important that $Fo_u \ll Fo_r$ so that the power in each of the 15 segments does not significantly spread into adjacent ones during a test, compounding the energy calculations and reducing the accuracy. The results in this case are $Fo_r = 0.241t$ and

$Fo_u = 2.955 \times 10^{-4}t$, which shows that for a given amount of plasma ON time, heat spreading is very good in the radial direction when compared to the u direction.

Also, for this experiment to have accurate results, the Biot number should be much less than 1, $Bi < 0.1$ [Incropera and DeWitt, 1996], meaning the cooling is limited by the convection, resulting in small radial thermal gradients in the dielectric wall. In the case herein, the main mechanism for energy loss to the surroundings is not fully understood or known, since there is not only energy loss from natural convection and radiation but also unavoidable intermittent contact from the coolant tubing to the dielectric wall, which creates a path for additional energy losses. Hence, an accurate value for the Biot number cannot be readily calculated. Instead, the energy loss to the surrounding will be measured and the Biot number estimated in calculations presented in the following text.

The RPS is equipped with a plasma cycling feature that makes for easy control of the plasma ON time. In this case, the unit was configured for 1 cycle of 6 seconds of plasma ON time. Included in the time is the plasma ignition period (~1.5 seconds for this condition) where there is very little to no power deposited on the dielectric. After ignition, the plasma quickly switches to an inductive mode and stable power is delivered to the plasma in the plasma region.

The exact amount of time the power supply is at full inductive power is of main interest and can be determined from a diagnostics tool programmed into the RPS controller. In this case, it is set to record output power from the power supply for every 100 milliseconds during the plasma ON cycle. These data are plotted in Figure 3.6, which shows the unit is at full inductive power for

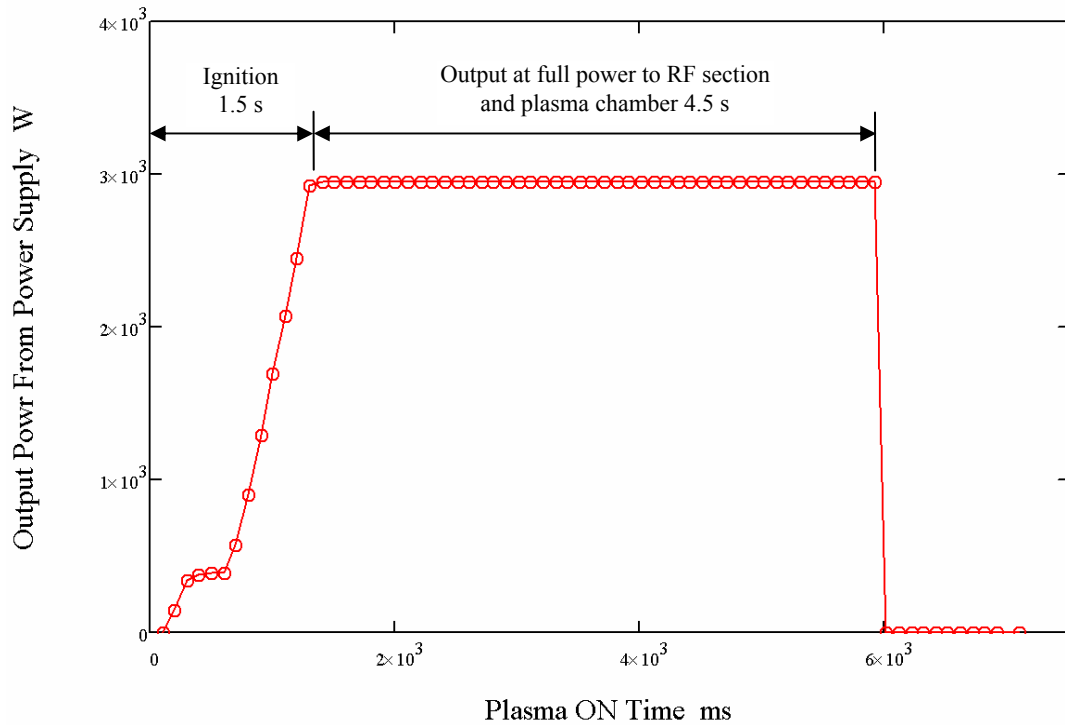


Figure 3.6 Output power from the power supply to the RF section and reactor for every 100 ms during the plasma ON cycle. This shows an ignition cycle of 1.5 seconds and 4.5 seconds of full inductive power.

4.5 seconds after the ignition cycle. This time will be called the Plasma ON time defined as $t_p=4.5$ seconds.

The unit was operated under identical plasma conditions as in Method 1 except for the short ON time. Specifically, the unit is operated for one 6 second cycle and thermal images captured every 150 ms for 30 seconds. The temperature for the hottest section (section 7) near the middle of the plasma region is plotted in Figure 3.7 and shows two important features. First, the bulk temperature in the section reaches a maximum after 7 seconds during the experiment. Second, there

is some cooling apparent from the temperature decay evident after 7 seconds when the plasma source has been off for 2.5 seconds.

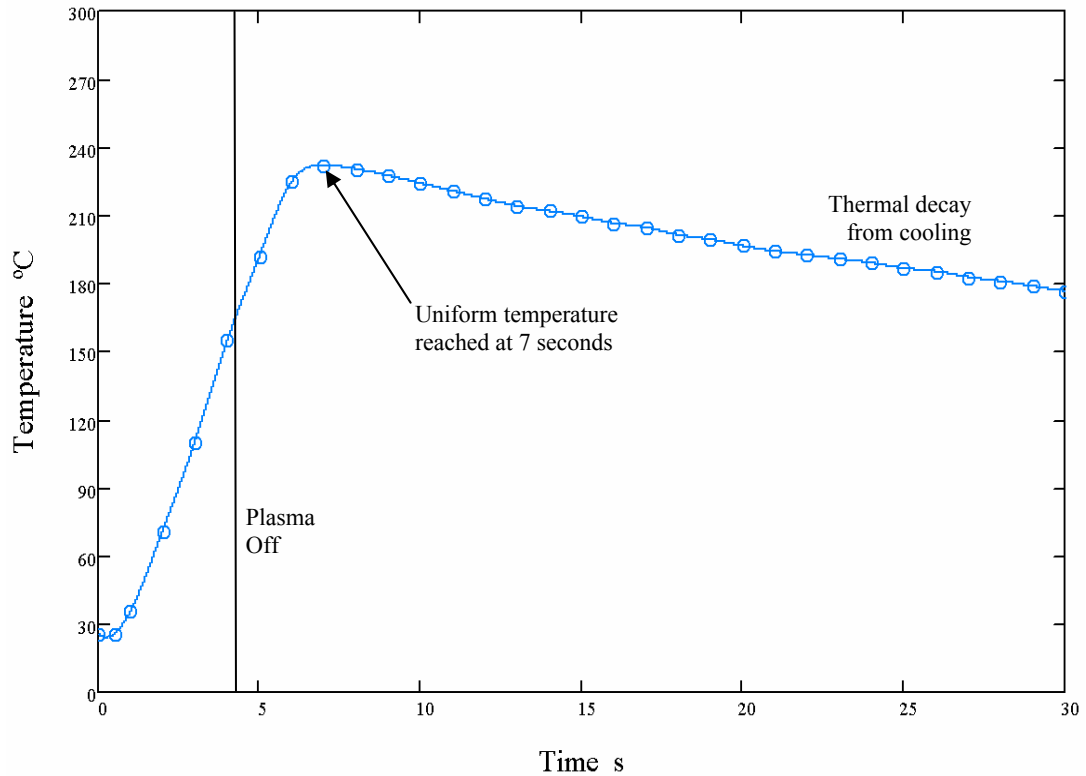


Figure 3.7 The temperature for the hottest section (section 7) near the middle of the dielectric. Uniform temperature is assumed to be reached in 7 seconds.

The temperature profile along in the u direction is shown in Figure 3.8 at 7 seconds when there is uniform temperature in the 15 sections. It is at this time when the energy calculations are made.

Now the energy in each segment is ready to be calculated. The net power to the volume, $\dot{E}_{net}(t)$ is defined in Equation 3.5 [Incropera and DeWitt, 1996]

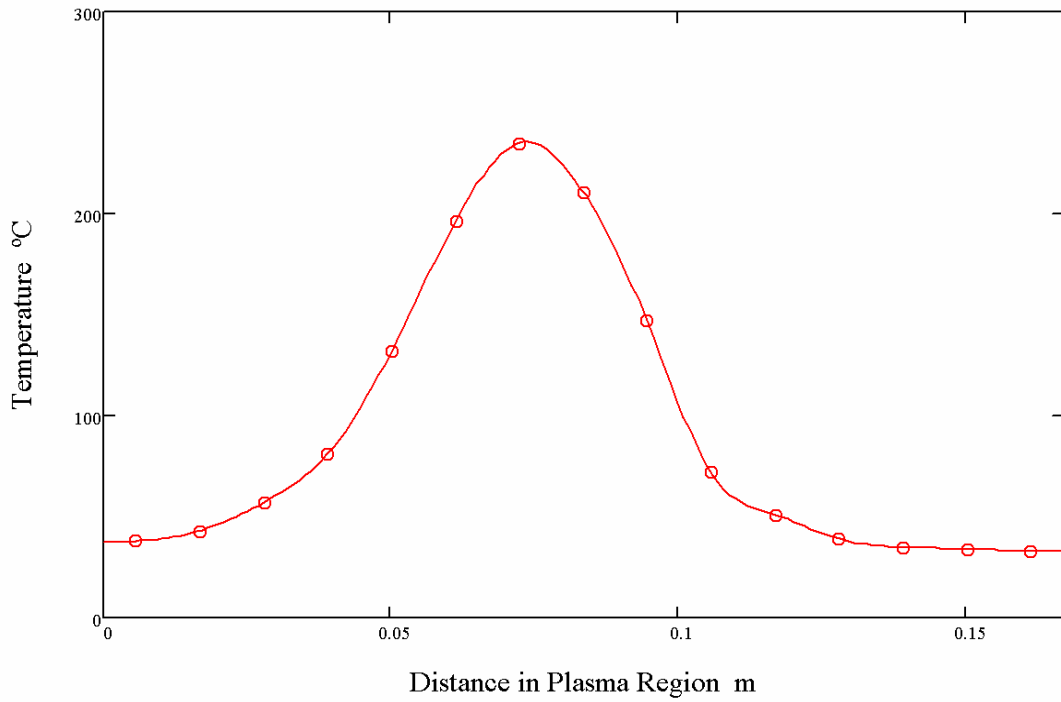


Figure 3.8 The temperature profile at 7 seconds when there is uniform temperature in the bulk volume.

$$\dot{E}_{net}(t) = \rho_{SiO_2} \cdot V \cdot Cp_{SiO_2}(T_q(t)) \cdot \frac{dT(t)}{dt} \quad (3.5)$$

where $\dot{E}_{net}(t)$ is in W, V is the volume of one segment of the dielectric, $T(t)$ is the temperature change above the ambient temperature and $T_q(t)$ is the bulk temperature of the volume, which at the 7 second time is also the surface temperature since the volume is assumed to be at uniform temperature. To calculate the net energy stored in the volume, $E_{net}(t)$ the net power is integrated with respect to time shown in Equation 3.6

$$E_{net}(t) = \rho_{SiO_2} \cdot V \cdot \int_0^t C p_{SiO_2}(T_q(t)) \cdot \frac{dT(t)}{dt} \cdot dt \quad (3.6)$$

where $E_{net}(t)$ is in J.

The energy into the volume is calculated by integrating the power applied to the volume during a specific time described in Equation 3.7. The integral is separated into two timeframes, $0 < t < t_p$ and $t > t_p$ where t_p is the plasma ON time. This was done because for this experiment, the plasma is not ON during the entire time t and consequently the second integral is 0 because $\dot{E}_m(t) = 0$ for $t > t_p$.

$$E_{in}(t) = \int_0^{t_p} \dot{E}_m(t) dt + \int_{t_p}^t \dot{E}_m(t) dt \quad (3.7)$$

To take into account the energy loss in Equation 3.1, E_{out} will be calculated from the temperature decay after the maximum temperature is reached in the bulk volume. The slope is used to calculate a decay constant for compensating the net energy stored, so the total energy in the volume $E_{in}(t)$ can be calculated. The energy loss decreases proportionally with the bulk temperature change in the volume and is an exponential decay. Since the decay is proportional to the bulk temperature, Equation 3.5 can be re-written for the power loss as

$$\dot{E}_{out}(t) = \frac{T_q(t)}{T_1} \left(\rho_{SiO_2} \cdot V \cdot C_{p_{SiO_2}}(T_{q1}) \cdot \frac{dT_1}{dt} \right) \quad (3.8)$$

where T_1 and T_{q1} are reference temperatures and $T_q(t)$ is the bulk temperature of the quartz at time t . If a decay constant, λ , is defined as

$$\lambda = \frac{1}{T_1} \cdot \frac{dT_1}{dt} \quad (3.9)$$

then Equation 3.8 becomes

$$\dot{E}_{out}(t) = -\rho_{SiO_2} \cdot V \cdot \lambda \cdot C_{p_{SiO_2}}(T_{q1}) \cdot T_q(t) \quad (3.10)$$

The decay constant is calculated and averaged during the time 10-30 seconds for the data shown in Figure 3.7. Also, T_{q1} will be the average quartz temperature during the same timeframe. If Equation 3.10 is integrated with respect to time, the energy lost can be calculated, $E_{out}(t)$ in Joules.

$$E_{out}(t) = -\rho_{SiO_2} \cdot V \cdot \lambda \cdot C_{p_{SiO_2}}(T_{q1}) \cdot \int_0^t T_q(t) dt \quad (3.11)$$

The net heat flux loss can be calculated by dividing Equation 3.10 by the surface area for one section, $A_{sw} = 2.272 \times 10^{-3}$ meters².

$$q_{out}(t) = \frac{-\rho_{SiO_2} \cdot V \cdot \lambda \cdot Cp_{SiO_2}(T_{q1}) \cdot T_q(t)}{A_{sw}} \quad (3.12)$$

This heat flux calculation is for the hottest section (section 7) where it is most accurate. The heat flux loss for the rest of the quartz tube sections are estimated by assuming $q_{out}(t)$ is proportional to the bulk temperature in each section and is calculated for each section, curve fit and plotted in Figure 3.9.

The Biot number mentioned earlier can now be estimated. To do this, the heat transfer coefficient to the surroundings, h is calculated by Equation 3.13 [Incropera and DeWitt, 1996] where $T(t)$ is the temperature change above ambient.

$$h(t) = \frac{q_{out}}{T(t)} \quad (3.13)$$

Again, working in section 7 at $t = 7$ seconds, the worst case (i.e. greatest) heat transfer coefficient is $h = 64 \text{ W}\cdot\text{m}^{-2}\cdot\text{°C}^{-1}$. This yields a value for Biot number equal to $Bi = 0.095$, which meets the $Bi < 0.1$ criteria for our assumption that the 15 sections of the dielectric wall are lumpable (i.e. lumped capacitance).

Substituting the different energy equations into Equation 3.1 and simplifying yields Equation 3.14; the power into a section at time t . The plasma power is integrated from 0 to t_p , hence the t_p in the denominator. The remaining

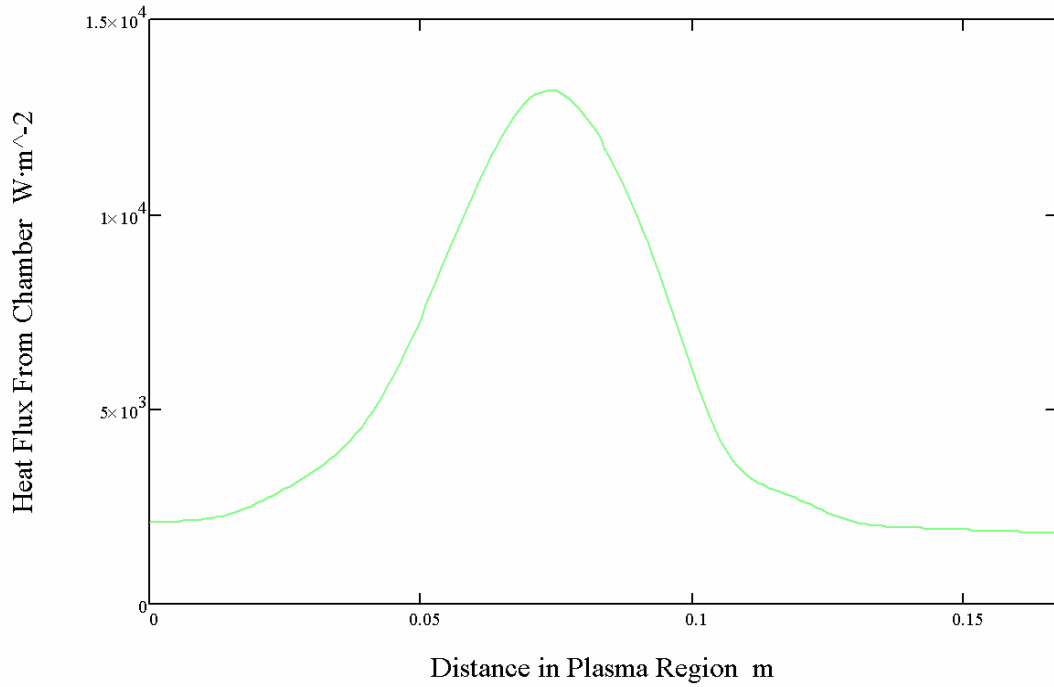


Figure 3.9 Heat Flux loss to the surroundings from the dielectric along the plasma region, q_{out} .

integrals are from 0 to t , where t is the time to the local maximum temperature in the volume. The time values were mentioned before and are $t = 7$ and $t_p = 4.5$ seconds, respectively.

$$\dot{E}_{in}(t) = \frac{\rho_{SiO_2} \cdot V \cdot \left(\int_0^t C_{p_{SiO_2}}(T_q(t)) \cdot dT(t) + \lambda \cdot C_{p_{SiO_2}}(T_{q1}) \cdot \int_0^t T(t) dt \right)}{t_p} \quad (3.14)$$

The heat flux into the volume, q_{in} , is calculated by dividing $\dot{E}_{in}(t)$ by the surface area for one section.

$$q_{in} = \frac{\dot{E}_{in}(t)}{A_{sw}} \quad (3.15)$$

The heat flux from the plasma to the quartz chamber is calculated for each section, curve fit and plotted in Figure 3.10. Also shown in the figure is the net heat flux which was not adjusted for losses to the surroundings.

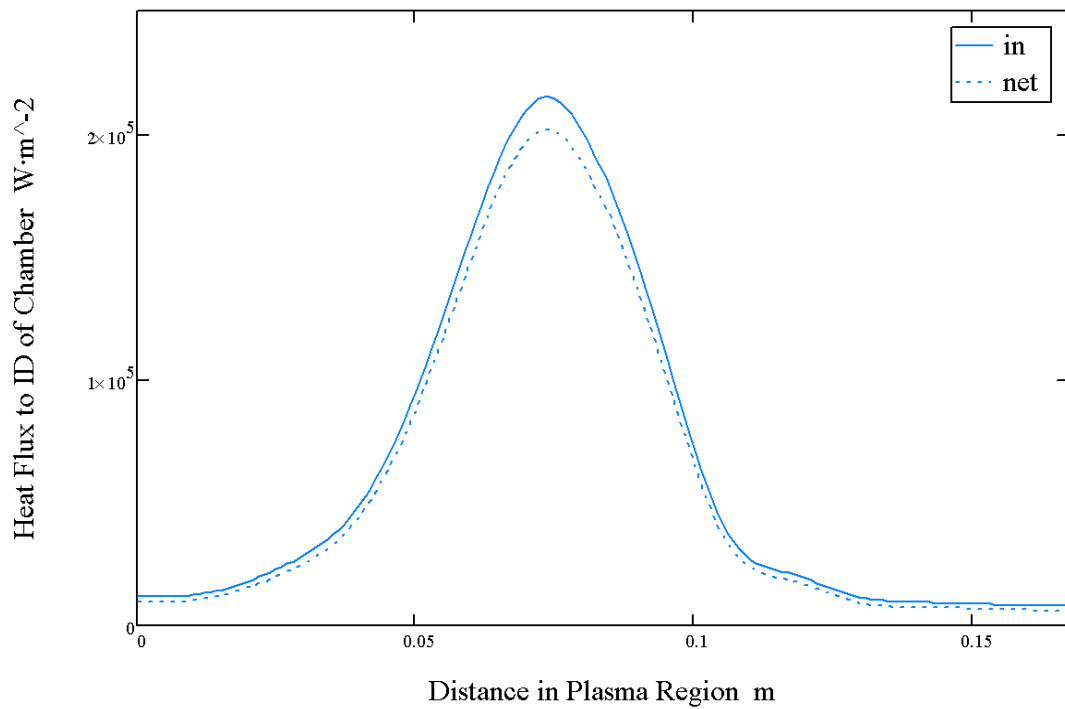


Figure 3.10 The net heat flux to the dielectric, q_{net} plotted with the total heat flux to the volume, q_{in} (includes the power loss) along the plasma region. This shows the adjustment made to estimate the total power q_{in} to the volume.

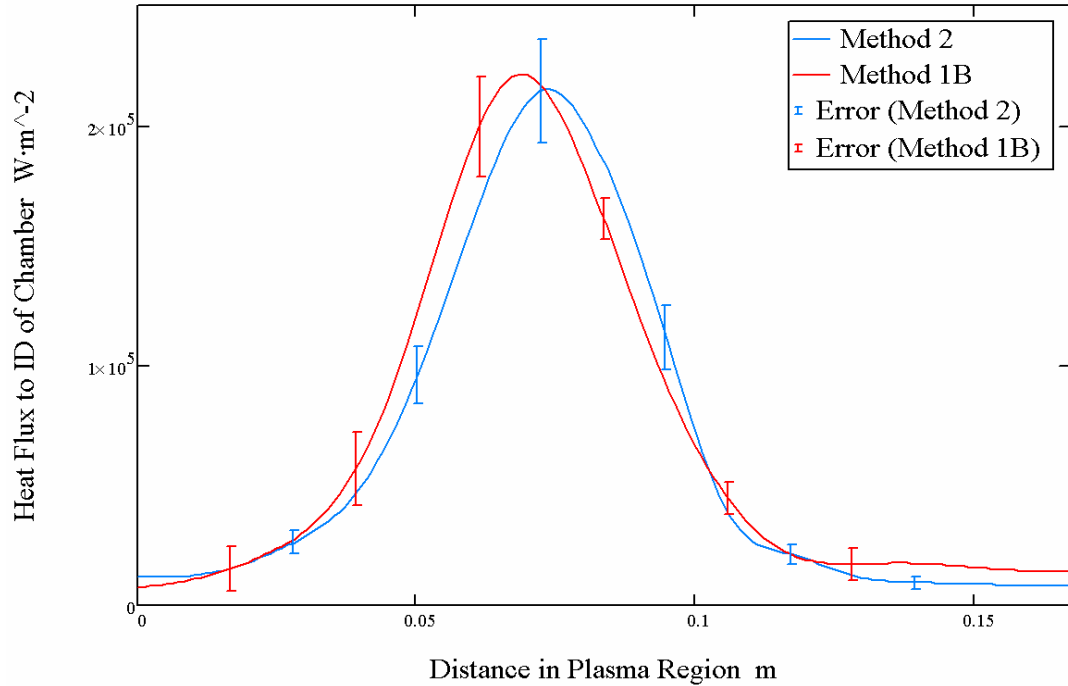


Figure 3.11 Plot of the total heat flux to the chamber wall, q_{in} for Method 2 compared with the results of Method 1B.

Figure 3.11 compares q_{in} for Method 2 with the results of Method 1B. The total power to the dielectric wall, from integrating the q_{in} curve for Method 2, is 2153 ± 50 W compared to Method 1B at 2342 ± 40 W. Although different in nature, both methods show consistent results, allowing for the determination of the spatially resolved heat flux from the plasma in different reactors designs. This information is of crucial importance for the optimal design of plasma reactors with high reliability and long chamber lifetimes. The next Chapter shows with examples how these results can be used in the design of cylindrical plasma reactors.

CHAPTER 4
APPLICATION OF HEAT FLUX DISTRIBUTION DATA IN REACTOR
DESIGN

4.1 Introduction

The difficulties in thermal management of plasma reactors where high density plasmas are present are most evident when existing technologies are pushed to higher powers. In many cases the limiting factor in reactor design is the ability to effectively manage the thermal energy transferred to the chamber wall from the plasma. The difficulties in constructing quantitative, self-consistent models of the energy transfer between the plasma and chamber wall forces the use of experimental approaches to measure the heat loads. The previous 2 chapters provide the means to extract spatial power distributions of heat from the plasma to the chamber wall from experimental data. This chapter describes how empirical heat load information can be used to improve ICP reactor designs.

From inspection of previous operational data of the dielectric chamber used in the experiments, it is evident that when the plasma power is increased; there is a limit where the chamber will fracture or fail. The cause of this failure mode is from non-uniform heat distribution leading to intolerable internal stresses due to temperature gradients and subsequent differential thermal expansions within the chamber material. While most chamber materials have high thermal operating temperatures that are tolerant of uniform distributions, they typically have poor thermal conductivity and poor resistance to high thermal gradients.

4.2 Experimental Reactor Failure

The failures due to fracturing of the dielectric chamber material are almost digital in nature and are very repeatable. This is due to the low yield characteristics of the dielectric materials used, usually quartz or ceramic. In the case of a cylindrical ICP reactor, it can be experimentally determined at what power level the dielectric chamber material will fail. These are costly experiments since the failures are irreversible. While the failure power level is repeatable for a single plasma condition created within a given gas species, it is not consistent for all plasmas conditions. For instance, two different plasmas, Ar at relatively low pressure compared to O₂ at relatively high pressure, will cause material failure at very different power levels. One can conclude that high pressure O₂ and low pressure Ar result in energy transport mechanisms to the wall which varies widely. In addition to this, the chamber material will have its own unique behavior to thermal stress, which is evident when comparing similar processes in quartz and alumina chambers.

Earlier versions of the reactor used herein will fail at roughly 3000W when operating an O₂ plasma at 2 Torr. The same chamber design will easily operate a 0.5 Torr Ar plasma at 3000W. These operating conditions are two experimental extremes. Focusing solely on the thermal stress of the material suggests there is a highly non-uniform heat load distribution for the O₂ plasma while the Ar plasma has a relatively more uniform distribution. Using the techniques outlined in this thesis (specifically Method 1B), it is apparent that the heat load for a 2 Torr O₂ plasma is highly concentrated near the center of the

reactor (between the RF power connections) and the heat load from Ar is more uniform along the length of the reactor as shown in Figure 4.1. This information can be applied as a boundary condition to a finite element analysis to determine the mechanical stresses present in the chamber for each operating condition.

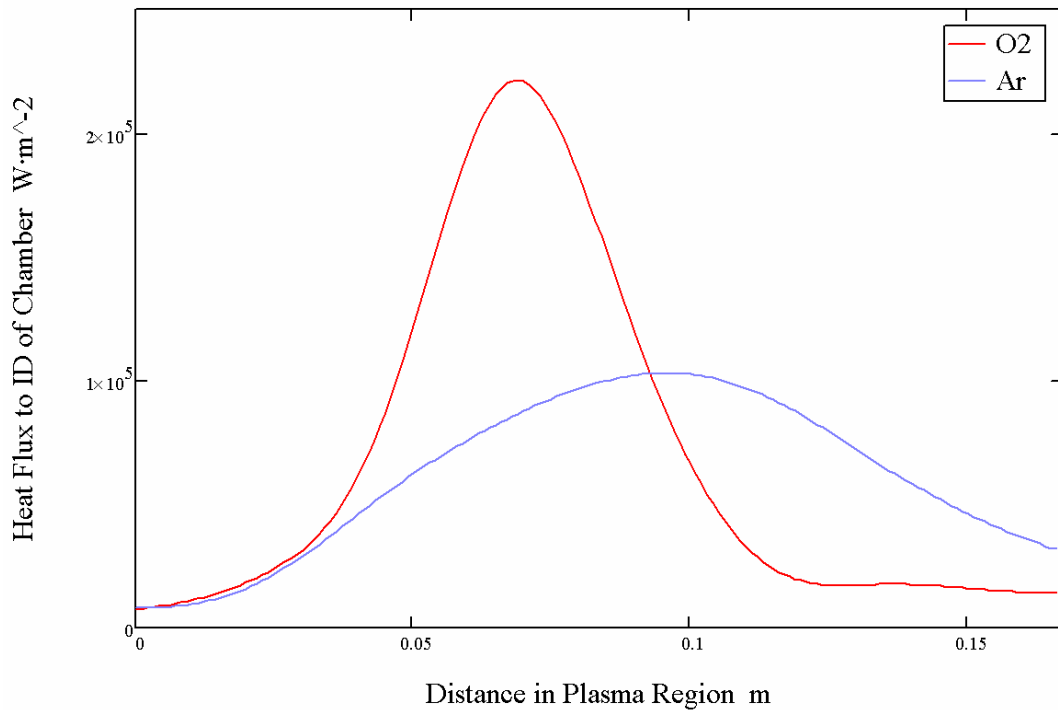


Figure 4.1 Heat flux distribution to the chamber wall in the plasma region for O₂ (750 SCCM, 2 Torr, 3000W) and Ar (250 SCCM, 0.1 Torr, 3000W). The heat flux from the O₂ plasma is much more localized compared to the Ar plasma.

4.3 Thermal-Mechanical Reactor Design Using Finite Element Analysis

Finite Element Analysis (FEA) is used to simulate temperature distributions and resulting thermal stresses in the dielectric material for a given plasma heat load. Two Finite Element Models (FEM's) are developed and discussed here for each of the conditions in Figure 4.1. These conditions are selected since they have well documented experimental data regarding chamber failures (or no failures) from the different plasma conditions for the same unique reactor design.

A 2D axi-symmetric FEM was developed using the reactor geometry and materials by way of the SDRC Ideas thermal modeling software. Using the same model, two different calculations were made for each of the heat loads, O₂ and Ar plasmas both at 3000W. The heat load boundary condition for the FEM was concentrated between the power taps for the O₂ plasma and was made more uniform along the length of the chamber for the Ar plasma as guided by the data in Figure 4.1. Under these conditions there are large thermal gradients near the areas of localized changes in the heat load as shown in Figure 4.2 for the O₂ plasma condition and consequently large corresponding stresses when these thermal data are applied to a stress model as shown in Figure 4.3. Alternately, the Ar plasma condition shows very gradual temperature changes and low stress concentrations. The ultimate strength of the dielectric material for this design is around 48 MPa and the FEM predicts stress failure for the O₂ condition. Conversely, the Ar condition results in stresses well below the ultimate strength

of the dielectric. Ultimately, these simulations show good correlation to experimental data and are able to predict failure from thermal stresses by proper application of heat from the plasma to the interior surfaces of the reactor.

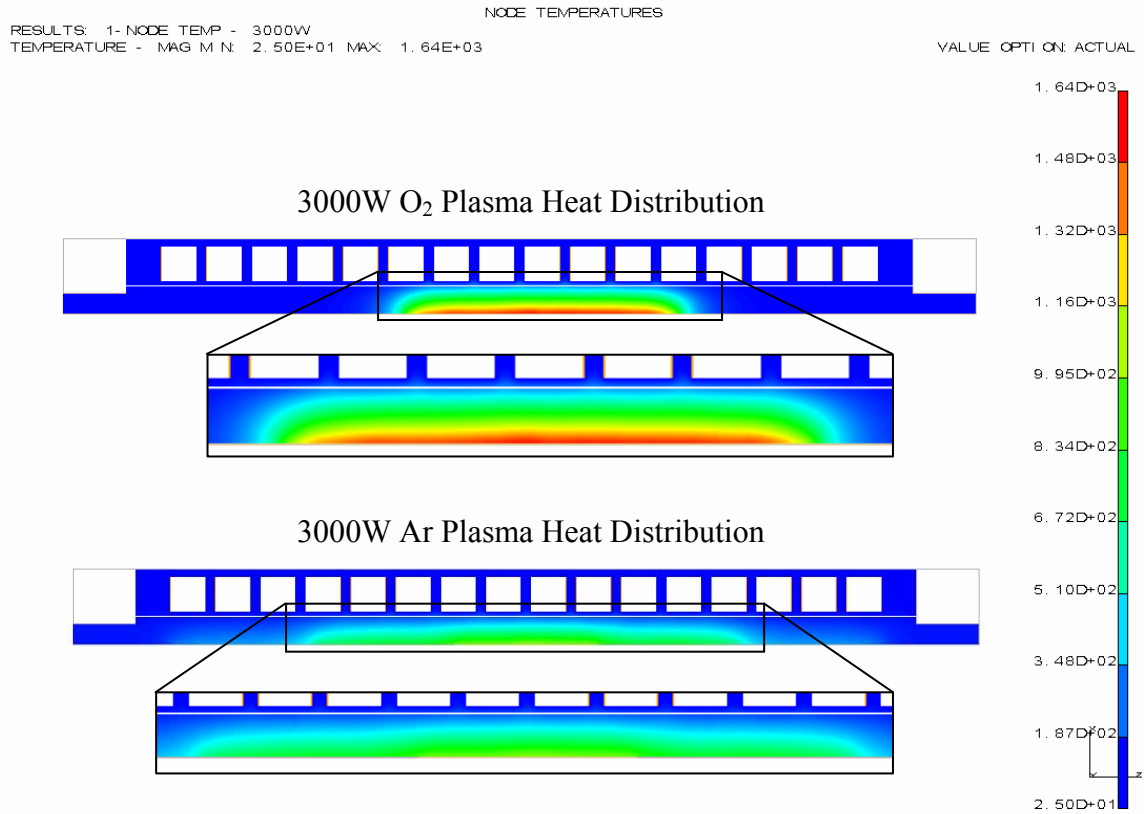


Figure 4.2 Thermal FEA simulation showing temperature distributions for two plasma conditions; O₂ and Ar, both at 3000W plasma power. The heat load distributions are similar to that of Figure 4.1 for O₂ and Ar.

D:\ideas_files\April_12_2004.rtf 1
 RESULTS: 3- B. C. 1, STRESS_3, RESTRAINT SET 1
 STRESS - VON MISES MIN: 3.90E+02 MAX: 5.55E+07
 FRAME OF REF: PART

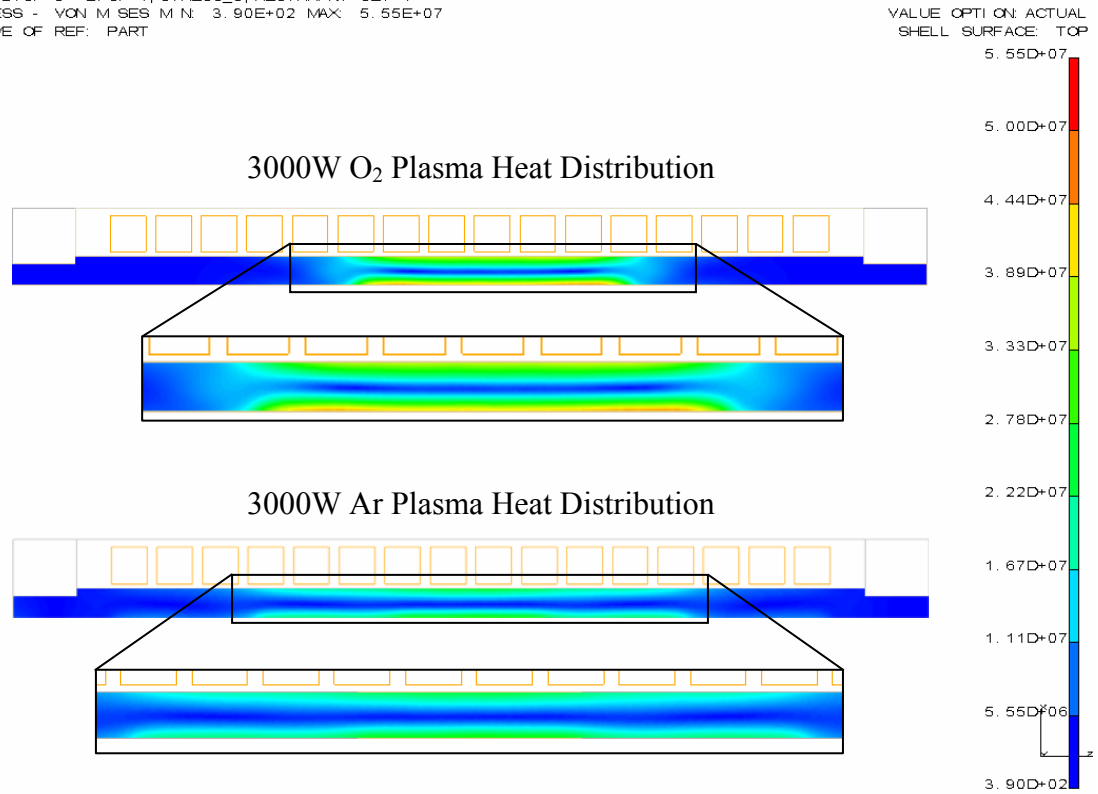


Figure 4.3 Mechanical stress FEA simulation showing the Von Mises stresses developed in the dielectric by the temperature distributions in Figure 4.2 for the two plasma conditions; O₂ and Ar. The ultimate strength of quartz is ~48 MPa.

Without the detailed knowledge of heat load distribution from the plasma, changes made to improve chamber reliability are not fully understood. For instance, in U.S. Pat. No. 6,156,667, the method of using a heat moderating material between the chamber and the cooling coil can be shown to have some positive affect in the overall attempt to optimize chamber resistance to high power densities. In one application of this method, the reliable operation of a 1200W

reactor increased to 1500W. While this improvement is notable, it is not fully understood nor optimized. Now, with full understanding of the plasma heat load characteristics, a more systematic approach can be taken to improve the reactor design. It can be shown that other aspects of the design have a much greater influence on the reliability and robustness than adding a heat moderating material. For instance, any combination of dielectric wall thickness, chamber tube diameter, proximity of the cooling coil to the chamber outer wall and use of thermal interface materials can have a significant impact on the thermal performance of a reactor. In the case of this ICP cylindrical reactor, the design that failed at 3000W in a O₂ plasma was optimized for operation at over 6000W (and has been proven up to 4500W to date).

Other aspects of reactor design are of an electrical power delivery and plasma production nature and involve features where the number of turns for the antenna, spacing between turns, diameter of the antenna, and the positions of the RF power connections are changed in one form or another to enhance the power coupling to the plasma or increase the reactor's operating range. The consequence of these changes on the mechanical performance of the reactor can be considered using the methods outlined in this thesis along with FEA.

CHAPTER 5

CONCLUSIONS

Two methods, not previously reported in the area of design of high performance inductive plasma sources were presented that allow the determination of the heat flux distributions to the plasma facing side of the dielectric tube in a cylindrical ICP reactor of arbitrarily small dimensions. Both methods possess unique advantages depending on the reactor design. Method 1, detailed in Chapter 2, is meant for reactors having relatively good thermal coupling to the coolant along with a high density of coolant tubing in contact with the dielectric. Its applicability is not limited by the material properties of the dielectric wall; specifically the thermal characteristics of the material will not affect that accuracy of the results. Method 2, developed in Chapter 3, is meant for experimental reactor designs where a coolant is not in thermal contact with the dielectric, however, as the accuracy of this method may be affected by heat spreading axially along the dielectric, its use for chamber materials with high thermal diffusivity should be avoided. The ICP reactor used for the experiments in this work lends itself to both methods due to its ease of modification. The results from Chapters 2 and 3 show that heat flux measurements using both methods under the same conditions are consistent. In addition, both methods show good agreement with independent determinations of total deposited power. Finally, spatially resolved temperature profiles obtained via computational fluid dynamics were found to agree closely with measured temperature distributions.

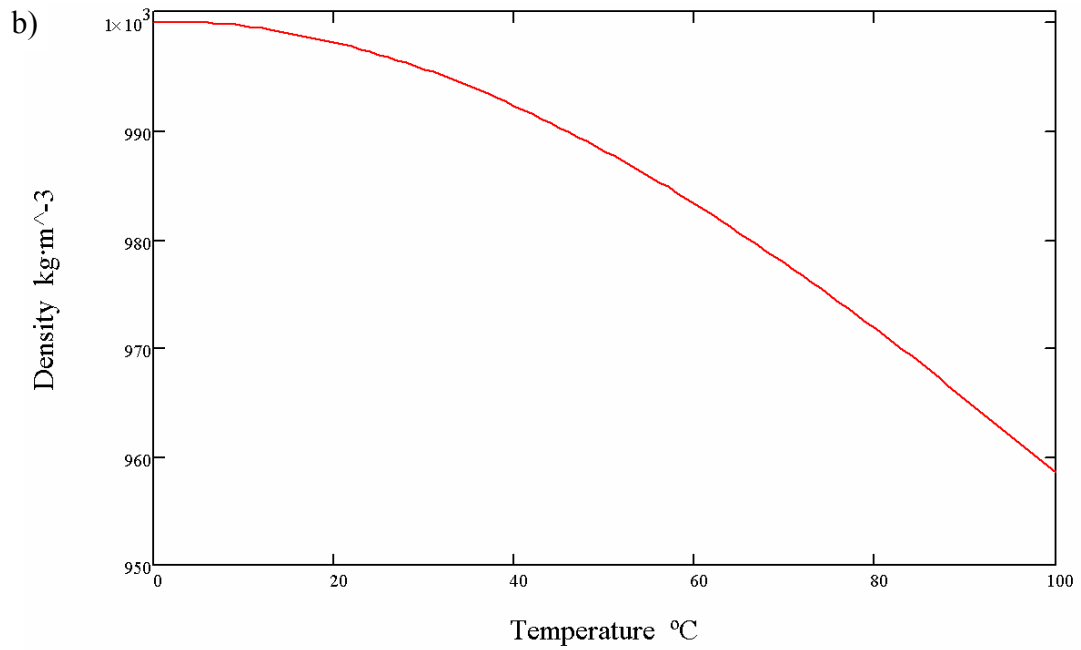
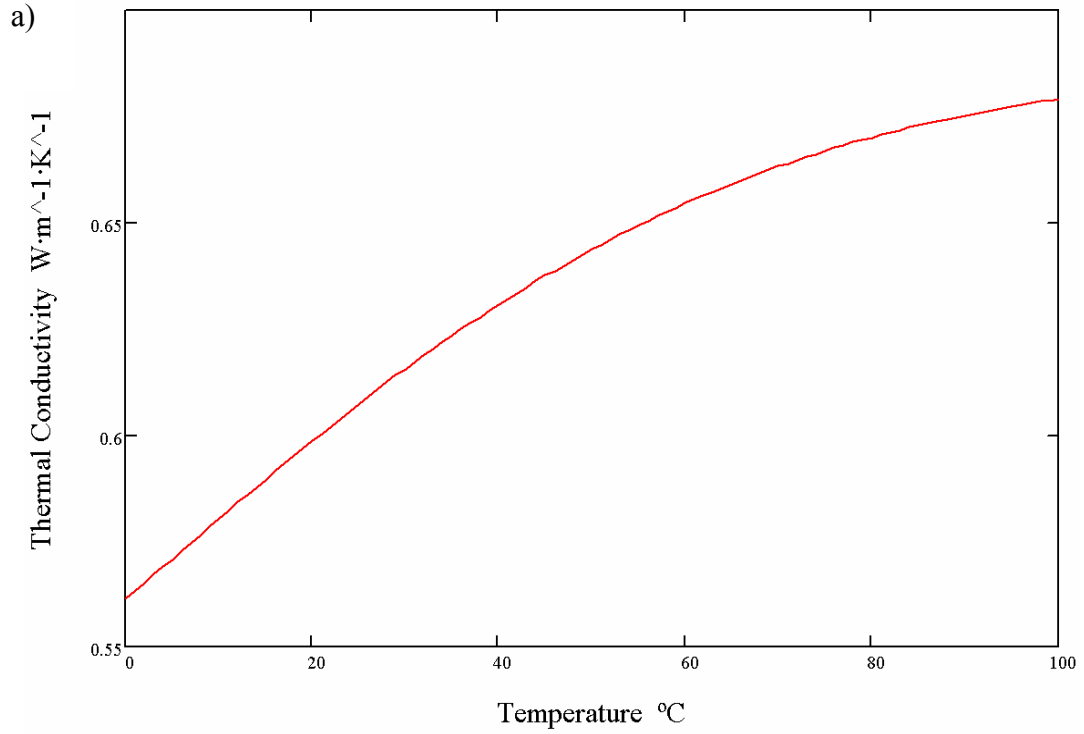
Since the determination of the heat flux does not involve probes internal to the chamber, these new methods are particularly suitable for the characterization and design of reactors of relatively small geometry where the plasma is difficult to access or can be easily disturbed. Also provided in this Thesis are examples of how the spatially resolved profiles obtained from these models can be used to predict internal stress resulting from the application of non-uniform heat loads that can lead to failure of the wall. Although motivated and developed for the particular case of cylindrical chambers, these methods can also be used in the study of chamber configurations other than cylindrical.

We now have two methods that experimentally determine the heat flux from the plasma to the chamber. Future work in this area could be used to advance the study of plasmas and the physical mechanisms of heat transfer at the plasma-surface interface. Other areas for future study could be centered on chamber design and sensitivity studies focusing on particular aspects of the heat removal. A sensitivity study on all the thermal interfaces (resistances) from the inside of the chamber through to the coolant, for example, could be useful to help determine the area of focus for enhance heat removal. This diagnostic tool may also provide useful information on the exploration and application of free-standing structures (i.e. liners) inside the plasma chamber and their affect on heat distribution and removal.

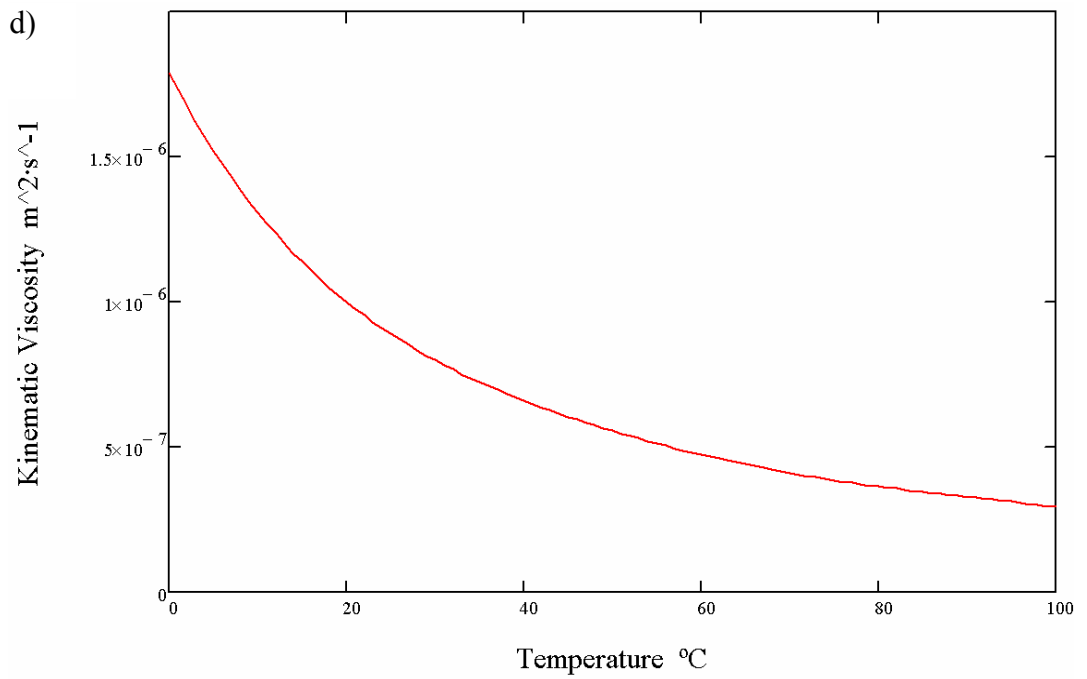
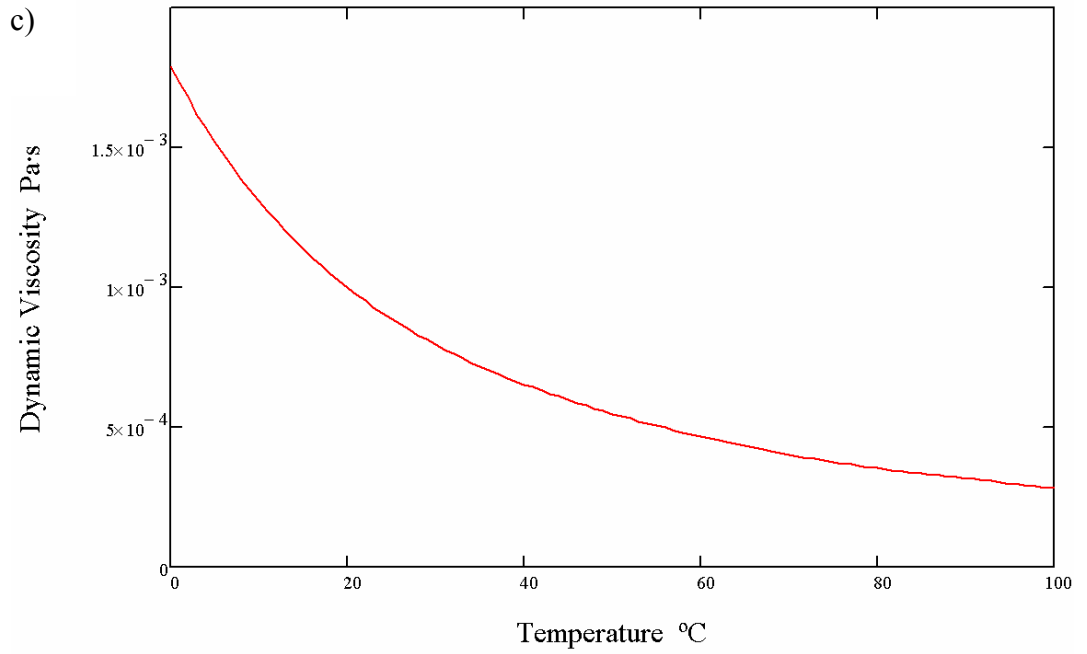
APPENDIX A

Isobaric Water Properties at 15 psia as Function of Temperature

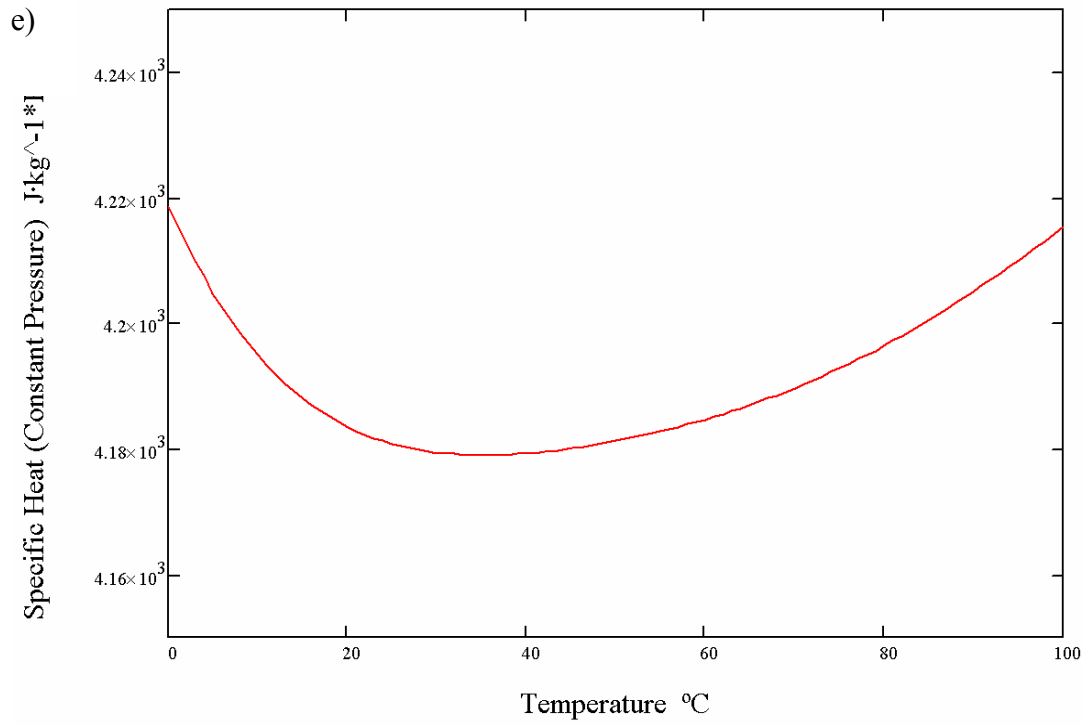
(Source: Online NIST Database)



NIST 15 psia isobaric water properties as function of temperature:
 a) Thermal conductivity b) Density



NIST 15 psia isobaric water properties as function of temperature:
 c) Dynamic viscosity d) Kinematic viscosity

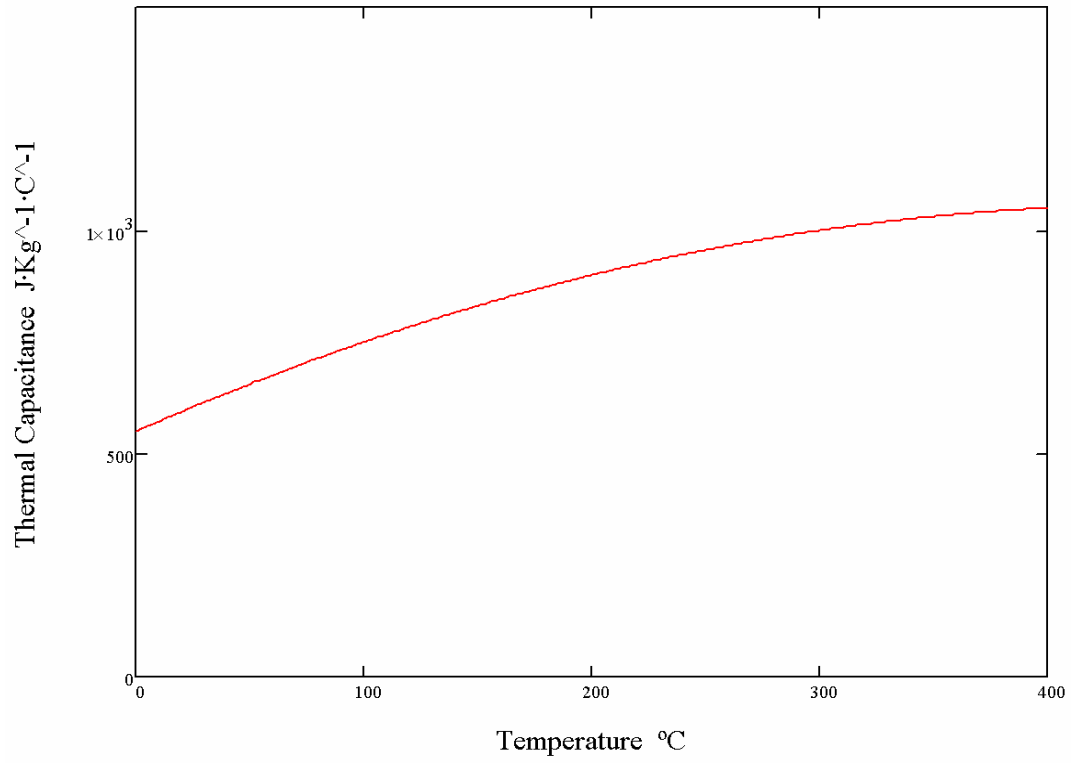


NIST 15 psia isobaric water properties as function of temperature:
e) Specific heat at constant pressure

APPENDIX B

Thermal Capacitance of Fused Quartz as Function of Temperature

(Source: Sosman R.B. (1927), "The Properties of Silica")



Thermal capacitance of fused quartz as a function of temperature